Studies on Microscale Defects

in Janus Monolayers

by

Shantanu Sinha

A Thesis Presented in Partial Fulfillment
of the Requirements for the Degree
Master of Science

Approved July 2022 by the
Graduate Supervisory Committee:

Sefaattin Tongay, Chair
Terry Alford
Sui Yang

ARIZONA STATE UNIVERSITY

August 2022

ABSTRACT

In the past decade, 2D materials especially transition metal dichalcogenides (TMDc), have been studied extensively for their remarkable optical and electrical properties arising from their reduced dimensionality. A new class of materials developed based on 2D TMDc that has gained great interest in recent years is Janus crystals. In contrast to TMDc, Janus monolayer consists of two different chalcogen atomic layers between which the transition metal layer is sandwiched. This structural asymmetry causes strain buildup or a vertically oriented electric field to form within the monolayer. The presence of strain brings questions about the materials' synthesis approach, particularly when strain begins to accumulate and whether it causes defects within monolayers.

The initial research demonstrated that Janus materials could be synthesized at high temperatures inside a chemical vapor deposition (CVD) furnace. Recently, a new method (selective epitaxy atomic replacement - SEAR) for plasma-based room temperature Janus crystal synthesis was proposed. In this method etching and replacing top layer chalcogen atoms of the TMDc monolayer happens with reactive hydrogen and sulfur radicals. Based on Raman and photoluminescence studies, the SEAR method produces high-quality Janus materials. Another method used to create Janus materials was the pulsed laser deposition (PLD) technique, which utilizes the interaction of sulfur/selenium plume with monolayer to replace the top chalcogen atomic layer in a single step.

The goal of this analysis is to characterize microscale defects that appear in 2D Janus materials after they are synthesized using SEAR and PLD techniques. Various microscopic techniques were used for this purpose, as well as to understand the

mechanism of defect formation. The main mechanism of defect formation was proposed to be strain release phenomena. Furthermore, different chalcogen atom positions within the monolayer result in different types of defects, such as the appearance of cracks or wrinkles across monolayers. In addition to investigating sample topography, Kelvin probe force microscopy (KPFM) was used to examine its electrical properties to see if the formation of defects impacts work function. Further study directions have been suggested for identifying and characterizing defects and their formation mechanism in the Janus crystals to understand their fundamental properties.

ACKNOWLEDGMENTS

I would want to convey my sincere appreciation to my advisor and mentor, Dr. Sefaattin Tongay, for letting me work with his team and taking full advantage of the resources he maintains. I have benefited so much from his vast expertise in studying 2D materials as a master's student. There isn't a more fantastic advisor I can think of who provided such strategic direction for each project I worked on at Arizona State University.

I particularly appreciate the group's members' invaluable ideologies and constant help with my work, especially M.S.Yasir, and K.Yumigeta. You guys supported me in my initial working days in Dr. Tongay's lab for research on 2D materials. With your help, I was able to learn the basics of research, synthesis, sample preparation, and characterization techniques that I have listed in this thesis. After that, I want to thank Dr. J.K.Kopaczek. Without your help, I wouldn't have finished this thesis, and with your consistent feedback and support, I have become a better researcher and greatly improved my presentation skills. Finally, without all of those insightful discussions with you and M.S.Yasir, I wouldn't have had such a different perspective on life; therefore, I cannot thank you enough for everything you've done for me.

Next, I would like to thank A. Yarra and S.T.R.Moosavy, you both not only helped with research but also supported me during challenging times in my academic and social lives. Thanks to our current members in the group: Taylan Görkan, Debarati Hajra, Rounak Banerjee, Patrik Hays, Renee Sailus, Blake Povilus, Sushant Lakhavade, Emmie

Benard, and Hayley Ruddick for all the insightful discussions. Finally, I would also like to thank all the alumni from this group: Dr.Ying Qin, Dr. Han Li, Dr. Yuxia Shen, Mark Blei, and Y.Attarde for their selfless help during my research.

Lastly, I am indebted to my beautiful parents and invaluable friends, who consistently provided moral support and stood by me during trying times.

TABLE OF CONTENTS

Page

CHAPTER Page

CHAPTER Page

LIST OF TABLES

Table Page

LIST OF FIGURES

Figure Page

Figure Page

Figure Page

Figure Page

Figure Page

CHAPTER 1: INTRODUCTION

1.1. 2D layered materials

Nanomaterials have been classified based on different properties, and one of them is the number of dimensions in material that are outside the nanoscale regime, i.e., less than 100 nanometers range. In the case of a zero-dimensional material (0D), all dimensions can be measured within the nanoscale, meaning these materials can be called nanoparticles [1]. For one-dimensional (1D) materials, one of the dimensions is outside the nanoscale range, as in the case of nanotubes or nanowires. Two-dimensional (2D) materials have only one dimension that is just a few atoms thick, while the other two dimensions are outside the nanoscale range, making these materials just surfaces [1]. These crystalline materials exhibit strong in-plane chemical bonding and a weak out-of-plane van der Waals interaction with two layers. Ever since graphene was isolated in 2004 by Andre Geim and Novoselov[2], a new perspective came to light among the scientific community towards 2D layered materials. A one-atom-thick graphene layer was isolated via mechanical exfoliation technique using a scotch tape on a Si/SiO_2 substrate. Owing to its remarkably high room temperature carrier mobility and environmental stability, the researcher saw it as a potential candidate for electronic applications in metallic transistors[2][3][4]. Isolation of graphene was followed by substantial research to probe its mechanical, electrical, and optical properties.

Graphene's electron mobility was found to be ($>10^5$ $cm^2v\text{-}^1s^{-1}$) [5], thermal conductivity (5000 Wm-1K-1) [6], and Young's modulus to be 1TPa [7]. Moreover, the

electronic band formation resembles Dirac cone features, leading to electronic properties like quantum transport of massless Dirac fermions, among various other relativistic phenomena [8][9][10].

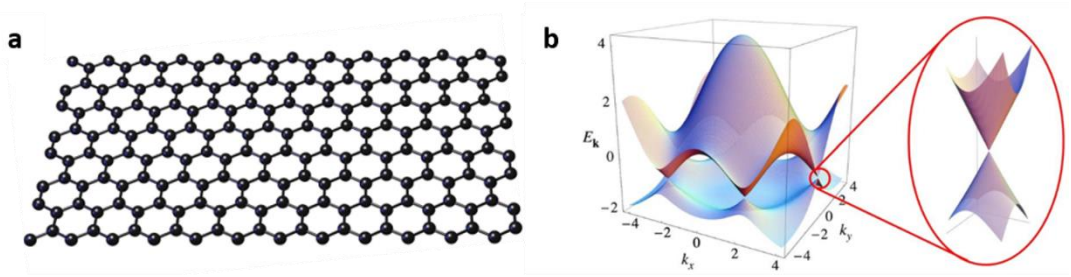

Fig 1. 1 a. The honeycomb lattice structure of Graphene. b. Dirac cone formation in electronic dispersion of graphene in the first Brillouin zone, zoom-in at the (π- and π+) bands near Dirac points [3].

Even though Graphene was successfully isolated and synthesized, the lack of bandgap made it difficult to be used in the field-effect transistor (FET) technology. The isolation of Graphene paved the way to the realization and eventual synthesis of a new category of "two dimensional materials" in which Transition Metal Dichalcogenides (TMDc) garnered the most attention within the scientific community. Since these materials were showed wide range of electronic and optical properties in their monolayer structure, these were envisioned to be of use in the field of optoelectronics as well as spintronics, owing to their tunable electronic bandgaps [11]. The interest in these materials picked up pace after the discovery of strong photoluminescence in MoS_2 monolayers, as one atom thick layer of MoS_2 exhibited properties of a direct bandgap material [12][13]. Their large bandgap (1-2eV) made them a promising candidate for FETs [14]. With the development

of CVD and CVT techniques, synthesizing high-quality monolayers, TMDc materials became an achievable possibility.

1.2. Transition Metal Dichalcogenides (TMDc):

TMDc materials with formula MX_2 (M representing transition metal like Molybdenum, Tungsten or Vanadium and X representing chalcogens like Selenium, Sulfur, or Tellurium) have been mainly studied with invested interest [15]. TMDc monolayer is composed of a layer of metal atoms sandwiched between two layers of chalcogen atoms bonded in a hexagonal structure. Monolayers of TMDc materials can be in the 1H or 1T phase, whereas for a few layers to bulk, the stacking structure can form either 2H (AB) or 3R (ABC stacking) phase [16].

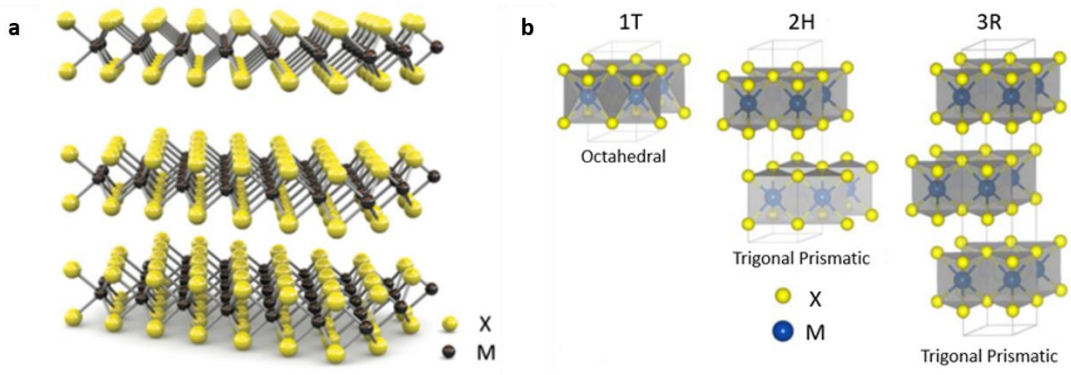

Fig 1. 2 a. Schematic showing TMDc structure [17]. b. Structural representation of 1T 2H and 3R stacking in TMDc [18].

The monolayers have shown to be stable under ambient conditions when exfoliated from the bulk crystals, where a weak Van der Waals bonding is present between the layers. The symmetry of few-layer MX_2 crystals depends on the number of layers in the structure, as D_{3h} point group is formed due to the lack of an inversion center in the

trigonal prismatic structure. For a structure having multiple numbers of layers, translational symmetry along the out of plane direction forms D_{6h} point group [19].

Material	Phase	Space Group		Point group	
		Bulk	N = odd	N = even	Bulk
$MoSe_2$, MoS_2	2H	$P6_3mmc^{-1}$	D3h	D3d	D6h
WSe_2, WS_2	1T	$P\bar{3}m_1$	D3d	D3d	D3d
$MoTe_2$, $SnSe_2$	3R	R3m	-	-	C3v

Table 1. 1 Phase, space, and point group for TMDc for different numbers of layers [20]

1.2.1. Properties due to structure and symmetry:

Bulk TMDc materials have been categorized as indirect bandgap materials. This is because the conduction band minimum (CBM) is located in the middle of Γ- K, in the first Brillouin zone, and the valence band maximum (VBM) is located at the Γ point, which is the center of the Brillouin zone [21]. As the crystal is thinned down to monolayer form, the indirect bandgap energy related to the gap between Γ- K points increases. In contrast, the CB and VB energies corresponding to the K± separation remain the same. Thus, a transition from an indirect bandgap to a direct bandgap is seen for the semiconductor TMDc monolayer, leading to a considerable increment in light emission intensity for the atomically thin layers. Applications in devices are much more promising when there is a direct bandgap in the system. Some device prototypes have

already been demonstrated, such as field-effect transistors, photodetectors, sensors, heterostructure junction devices, and more [22].

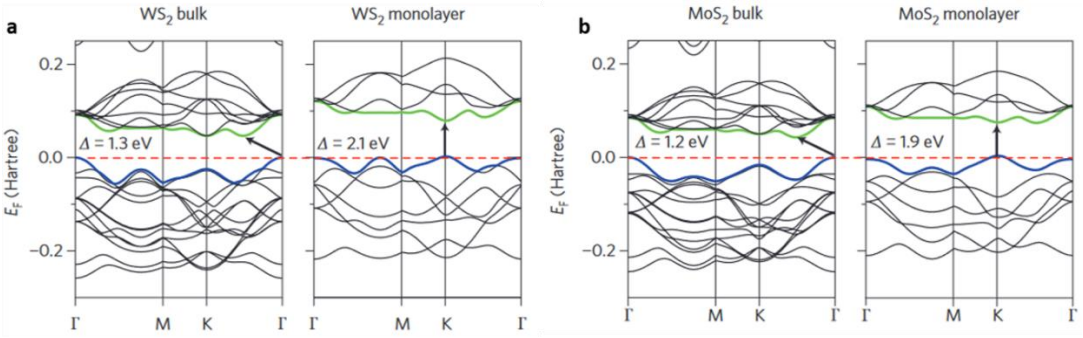

Fig 1. 3 a. Electronic bandgap for Monolayer and bulk WS_2. b. Electronic bandgap for MoS_2 bulk and monolayer. Calculations have been done through density functional theory (DFT) [14].

Monolayer TMDc indicate the existence of a stronger spin-orbit coupling compare to that of graphene [23]. This can be attributed to the fact that spin-orbit interaction is a relativistic effect and is more prominent in TMDc because of the higher atomic number of elements present in the TMDc, besides the participation from d-orbitals of the transition metals [24]. Weak dielectric screening from the surroundings can be held accountable for amplifying the coulombic interaction detected in the 2D monolayers. The Coulomb interactions in TMDc monolayers facilitate the formation of bound electron-hole pairs (excitons) having binding energies around 0.5 eV. The optical and spin properties observed at room temperature as well as at cryogenic temperatures are heavily dominated by the formation of excitons in these materials.

The Electronic Bloch States of a material are governed by its crystal symmetry [25]. Out of many fascinating properties, here two are being discussed, which resulted from the

broken inversion symmetry in monolayer MX_2 systems. First, for monolayer MoS_2, it was observed that momentum space valleys are spatially separated even though there are two energy degenerates for valence and conduction band edges. Because of disparate selection rules for K+ and K- valleys, monolayer MoS_2 photoluminescence is found to be circularly polarized. This feature can be exploited in applications for quantum computing or valleytronics [26][27].

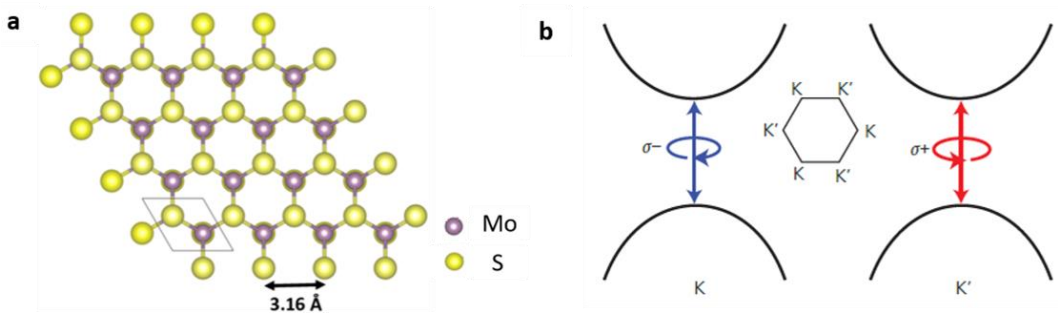

Fig 1. 4 a. Schematic for MoS_2 monolayer structure having no inversion symmetry. b. Schematic demonstrating selection rule for valley-dependent polarization.

Through the piezoelectric effect, the applied stress on material results in the generation of electric charge and vice-versa [28]. Piezoelectric materials are widely used in actuators, energy harvesting devices, and mechanical sensors. Though inversion center in a material's crystal structure, as in the case of monolayer TMDc such as MoS_2, can nullify the polarization generated due to the symmetry operation. Hence, only an odd number of layers in the MX_2 system are known to exhibit this phenomenon [14].

1.3. Molybdenum and Tungsten based TMDc

In bulk form, TMDc is found in various polyforms such as 1T (Trigonal), 2H (Hexagonal), and 3R (Rhombohedral). [24][29] Whereas, in monolayer forms such as WS_2, WSe_2 are found in just two polymorphs, Trigonal Prismatic and Octahedral [30]. At equilibrium, tungsten and chalcogen atoms in WX_2 (X= S, Se) TMDc form a hexagonal lattice structure, belonging to the symmetry group D_{3h}. Both WS_2 and WSe_2 are indirect bandgap materials in bulk forms [31]. It is observed that at the Valence band maximum (VBM) Γ-point and Conduction band minimum (CBM) along the S-Γ path, an indirect bandgap is formed. Here, for bulk WS_2 (0.909 eV), the energy gap is marginally higher as compared to that of the bulk WSe_2 (0.826 eV) [32].

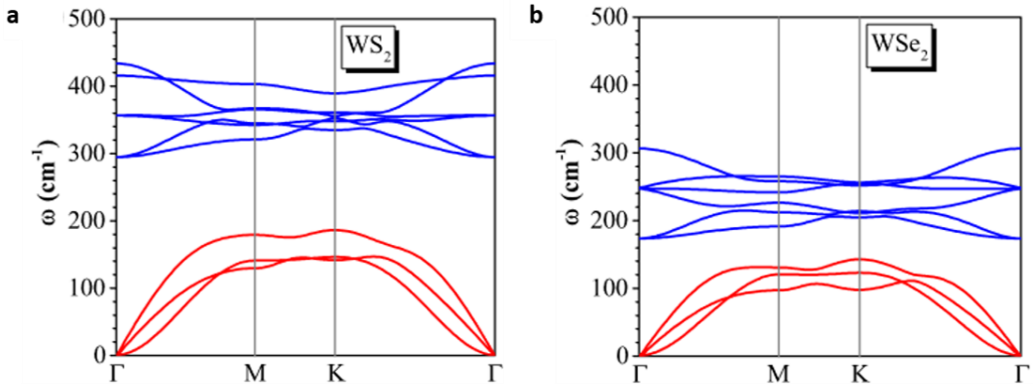

Fig 1. 5 a. Phonon dispersion models for WS_2. b. WSe_2 monolayers[33].

The electronic properties of the bulk MX_2 change drastically upon shifting from bulk to monolayer form, and this change in properties can be attributed to the quantum confinement effect. Due to this effect, a shift is seen from indirect to direct bandgap in the monolayer regime. Nevertheless, the monolayers are stable in their equilibrium state, as is apparent from Fig 1.5 (a, b), confirming no imaginary modes for the phonon

spectrum of monolayers of WS_2 and WSe_2. At equilibrium, results from the First principal calculations indicate bandgaps for monolayers of WS_2 and WSe_2 to be 1.800 eV and 1.566 eV, respectively [34].

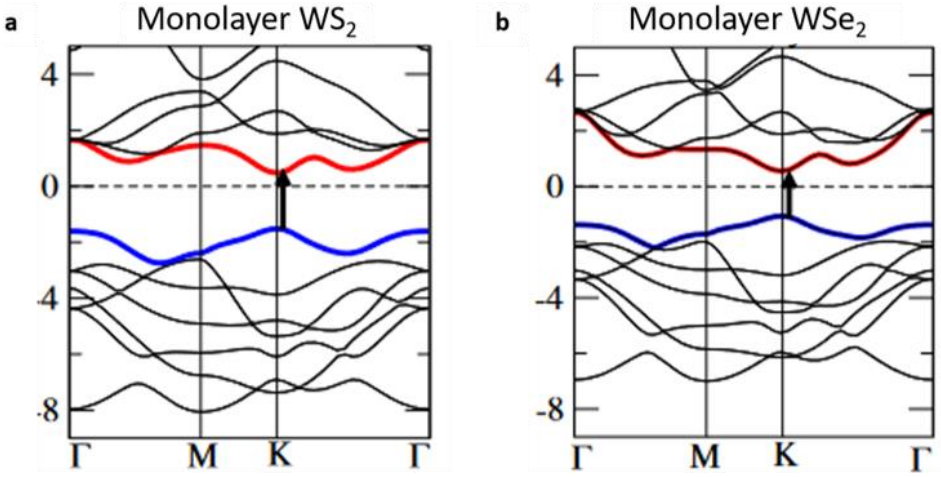

Fig 1. 6 electronic band structure of monolayer TMDc, determined via DFT; a. WS_2 and b. WSe_2 [34].

For device applications, WSe_2 has been used to form diodes with switchable polarity and transistors, which can be reversibly modified with the possibility of reconfiguring the carrier types [35]. A non-volatile homojunction was created using WSe_2 by manipulating the ferroelectric polarization of a BiFeo3 substrate underneath it, indicating the possibility of forming laterally two-dimensional electronics and photonics [36]. Additionally, with Ni-doped WSe_2 crystals, ferromagnetism at room temperature has been observed [37]. Similarly, a three times increase in photocurrent has been reported for phototransistors based on WSe_2 surface-functionalized with cesium carbonate. The results indicate a significant enhancement in device characteristics and performance [38]

The other most well-known example of TMDc material is the molybdenum disulfide (MoS_2). It is a layered material with strong in-plane bonds but weaker out-of-plane vdW interactions. R.F.Frindt isolated the monolayers of MoS_2 via liquid-assisted exfoliation for the first time around the late eighties [39]. However, at that time, these monolayers were only used as substrates for studying and characterizing organic molecules through scanning tunneling microscopy (STM) till the late 2000s [40][41][42]. Around 2010, MoS_2 was considered a potential candidate for studying the semiconducting nature of anatomically thin materials. Interest in MoS_2 was due to the possibility of a direct bandgap in it's monolayers [13].

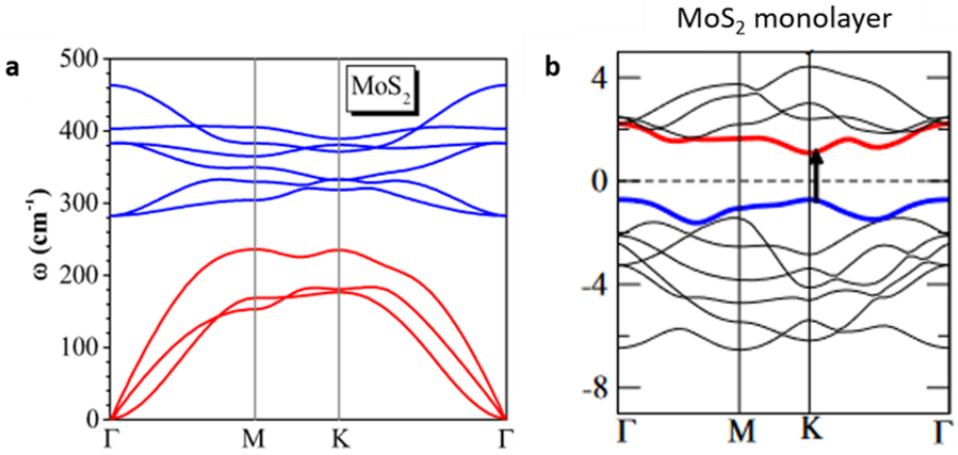

Fig 1. 7 a. Phonon dispersion relation for MoS_2 monolayer, calculated via DFT [33]. b. Electronic band structure for MoS_2 monolayer system [34].

MoS_2 has been one of the most widely investigated materials because of its potential applications in flexible electronics [43], lithium-ion batteries [44], valleytronics, and FETs [45][46]. In addition, Monolayer MoS_2 can be obtained by mechanical or liquid-assisted exfoliation, similar to how graphene was exfoliated [47][48].

Through mechanical exfoliation, trigonal prismatic (H-MoS_2) structure is obtained, showing semiconducting nature. In ambient atmospheric conditions, confirmed through Density Function Theory, trigonal prismatic H-MoS_2 is the most stable configuration having the space group P6/mmc [49]. The octahedral configuration of 2D MoS_2 was obtained through liquid-assisted exfoliation [50]. The bandgap for H-MoS_2 is 1.67 eV, while the T-MoS_2 having the octahedral configuration is metallic [51]. The industrial-scale synthesis of two-dimensional TMDc is mainly done using epitaxial techniques like Molecular beam epitaxy, vapor deposition methods such as Chemical Vapor Deposition (CVD), Physical Vapor Deposition (PVD), and other available techniques. Exfoliation methods only provide a quasi-two-dimensional structure that cannot yet be used for large-scale industrial applications.

The other Mo-based TMDc, one of the most promising materials in optoelectronics and microelectronics, is $MoSe_2$ [52]. It displays semiconducting behavior in its 2H phase, holding trigonal prismatic D_{3h} symmetry [53]. When isolated into monolayers, it transitions into a direct bandgap material displaying a bandgap of 1.55 eV, as compared to its bulk crystal exhibiting a 1.1 eV bandgap [53]. By applying mechanical strain or an external electric field, the bandgap in MoSe2 can be tuned. Given its broader optical absorption spectra, it is one of the most promising materials for light-emitting diodes, FETs, and other optoelectronic devices such as photodetectors [54]. Recently $MoSe_2$ has been enthusiastically studied for hydrogen evolution reactions (HER) owing to its mechanical stability and abundant active sites [55][56]. Application in photonic devices such as saturable absorbers (SA) is still being researched in $MoSe_2$-InSe heterostructures. These SAs show a higher signal-to-noise ratio in Q-switched fiber lasers than other

conventional fiber lasers [55]. P. Tonndorf first performed mechanical exfoliation to produce a monolayer of $MoSe_2$ and eventually detected strong photoluminescence indicating direct bandgap emission [57]. Even though there are many routes available for monolayer syntheses, such as CVD [58], molecular beam epitaxy (MBE) [59], intercalation stripping [60], and mechanical exfoliation; the semiconductor industry is yet to find a cost-effective and stable procedure to mass-produce large area $MoSe_2$ monolayer sheets.

1.4. Other TMDc Materials:

Other anisotropic materials besides Mo or W-based TMDc have also been studied for their intriguing optical, electronic, and structural properties. For instance, ReS_2, a recent addition to the TMDc family, is found in distorted 1T or 1T' phase giving it an in-plane anisotropy along with weak interlayer vdW interactions. ReS_2 is a flexible semiconductor whose optical, electronic, and magnetic properties can be tuned by doping or strain engineering [61]. Both ReS_2 monolayer and bulk are direct bandgap materials, with a bandgap of ~1.55 eV for monolayer and ~1.47 eV for bulk [62]. This unique feature in ReS_2 distinguishes it from other TMDc materials as both monolayer and bulk remain direct bandgap materials. This feature in $NbSe_2$ can be attributed to the lack of interlayer registry, weak interlayer coupling, and absence of band renormalization while transitioning from bulk to monolayer structure [63]. ReS_2 monolayer contains metal-chalcogen and metal-metal bonds, and the presence of a heavier transition metal spin-orbit coupling is very strong. Due to the Peierls distortion, the zig-zag formation of Re

chains breaks their hexagonal symmetry, and chalcogen and Re atoms are pushed out of the plane and thus create in-and out-of-plane anisotropy along the lattice vectors [64]. Due to the triclinic crystal structure, the optical absorption in ReS_2 becomes polarization-dependent [65]. The unique properties found in ReS_2 make it a promising candidate for thin-film transistors TFTs; also, it provides more active sulfur edges, making it useful for lithium-ion batteries [64].

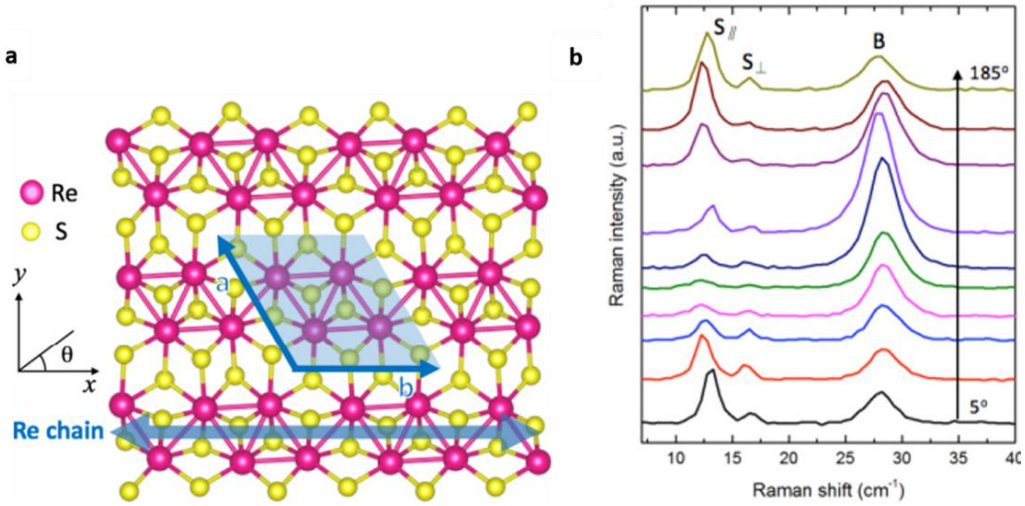

Fig 1. 8 a. Schematic for atomic configuration of monolayer ReS_2 showing 1T' phase. b. Raman spectra for shearing and breathing mode at different polarization angles (θ = 5°-185°) [66].

$NbSe_2$ is another fascinating TMDc studied for its superconductivity and enhanced charge density wave [67]. $NbSe_2$ monolayers behave as an intrinsic superconductor, exhibiting Ising superconductivity without any unique substrate. Characterization of transport properties of $NbSe_2$ revealed that at superconducting transition temperature *Tc* from 4.5K for a 10-layer sample to 1.0 K for a 2H-phase monolayer [67]. The other phenomenon which highlights $NbSe_2$ is the increment in charge-density-wave transition

temperature. Charge density waves are periodic fluctuations in charge densities caused by periodic lattice distortions at certain low temperatures [68]; for $NbSe_2$, charge density wave transition temperature changes from 33 K in bulk to 145 K in monolayer. This change can be attributed to the electron-phonon coupling seen in monolayer $NbSe_2$ [69]. These phenomena make $NbSe_2$ a valuable material for developing super-capacitors, oscillators, spintronics, and other electronic devices.

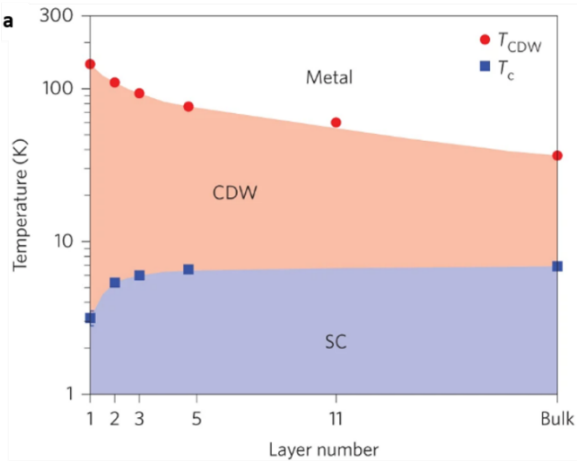

Fig 1. 9 Thickness vs temperature phase diagram for $NbSe_2$ [69]

List for such TMDc materials like $MoTe_2$ [70], TiS_2[71], and $ReSe_2$[72] goes on, which have tremendous potential for applications in logic circuits, photodetectors, sensors, and more, owing to their optical, electronic, and magnetic properties emerging from reduced geometry.

1.5. TMDc Janus Materials

Monolayers of transition metal dichalcogenides are known to be stable in the ambient environment. They are also semiconducting in nature and have a wide range of photo absorption spectrum. Even after having so many excellent properties, these materials can still be improved for their photocatalytic reactions and conversion efficiency [73]. The recently synthesized, asymmetric, and polar structure having a broken mirror symmetry courtesy of two different atomic species on either of the facets of a monolayer, termed as Janus, is one of the possible solutions to the challenges faced by TMDc materials.

Janus was the name of a Roman god, signifying future and past with one head in each direction. The name aptly describes Janus materials as the structural changes transform a classical TMDc into a new class of 2D material with different atomic species on the upper and lower sides of the material. [74]. Symmetry broke Janus materials exhibit phenomena such as ferromagnetism and ferroelectricity [75]. Janus materials based on the transition metals such as Molybdenum (Mo) and Tungsten (W) are being extensively researched [76]. Group-VI chalcogenides-based Janus materials have C_{3v} symmetry due to the MXY configuration. Due to the substantial difference in the electronegativities of atomic species forming these materials, a large electric field or vertical polarization is formed in Janus systems [74].

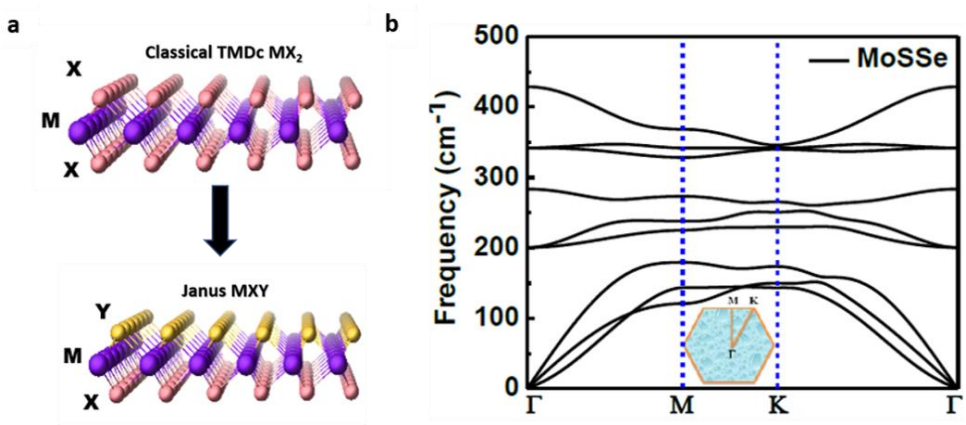

Fig 1. 10 a. Schematic representation of the transformation of a classical TMDc system to Janus material [74]. b. phonon band structure of Janus SeMoS monolayer; inset - Brillouin zone in conjunction with high symmetry points [77].

1.5.1. Exciting properties in Janus Materials

It was proposed that in Janus structures, broken mirror symmetry of the crystal system will lead to Rashba splitting of the valence band maximum at Γ-point [78]. Rashba splitting is the momentum-dependent splitting of spin bands, an effect caused by the spin-orbit interaction and asymmetric electric field potential in the orthogonal plane [79]. Applying an external electric field in the collinear direction to the built-in e-field generated in the MXY system due to the difference in electronegativity can enhance the spin splitting effect. Research studies on Janus SeMoS and SeWS materials and their heterostructure have confirmed the spin splitting effect in these materials. Broken mirror symmetry in Janus introduces an out-of-plane polarization field, which has been shown to stabilize spin-nondegenerate states at Γ point, leading to a strongly induced Rashba splitting effect. The anisotropic Rashba splitting can be enhanced remarkably by subjecting the Janus materials to compressive strain [80]. Changing the interlayer

distance in a bilayer MXY material can also be used to tune the layer-dependent Rashba splitting [81]. Thus in such a system where spin degeneracy is absent, an opportunity to manipulate independent electron spin opens applications in quantum devices and spintronics [82].

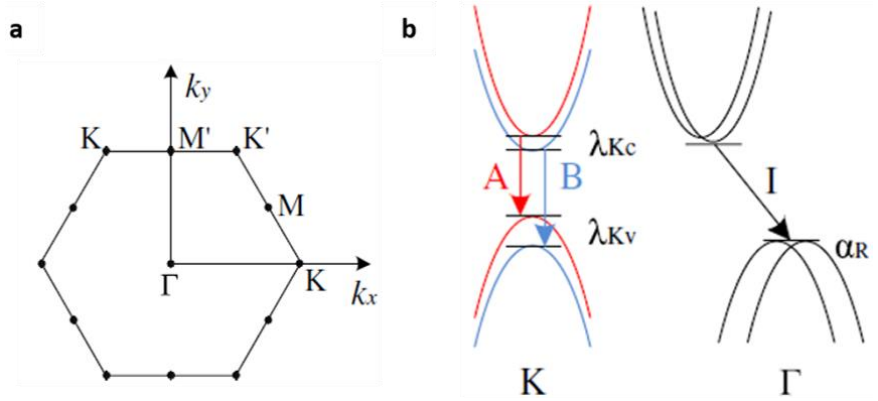

Fig 1. 11 a. Brillouin zone of MXY monolayer. b. Simulated electronic band structure. αR stands for the Rashba splitting of valence band at Γ point [78].

In Janus TMDc, the presence of two different atoms on either facet creates an electronegativity difference between the top and bottom layer, resulting in asymmetric dipole formation and a colossal vertical electric field inside the 2D structure. Due to the polarization field, a potential difference between the top and the bottom layer is predicted to be ~ 0.5 eV [83]. In ferromagnetic Janus materials such as CrIBr and SeVS, intrinsic polarization can enable high Curie temperature (Tc) ferromagnetism. Furthermore, a study suggests that the polarization field modulates the Dzyaloshinskii–Moriya interaction (DMI) strength. These properties open a path for memory devices utilizing spin manipulation [84].

New quantum device applications are possible with properties emerging from broken mirror symmetry and forming a permanent dipole in Janus materials. It is predicted that the Janus TMDc homojunction structure can form type-II junctions [85]. In these structures, the band offset is comparable to the potential difference between the top and bottom facets of the Janus sheet [85]. By tweaking the stacking order of Janus monolayers, valleytronic responses and large berry curvature values (~100 $bohr^2$) can be achieved [86][87]. Even without applying magnetic or electric fields or doping, the intrinsic properties of a Janus monolayer provide an opportunity to reach a 100 percent valley polarization. This phenomenon can show a way to tune spin polarization without applying external magnetic or electric fields [83].

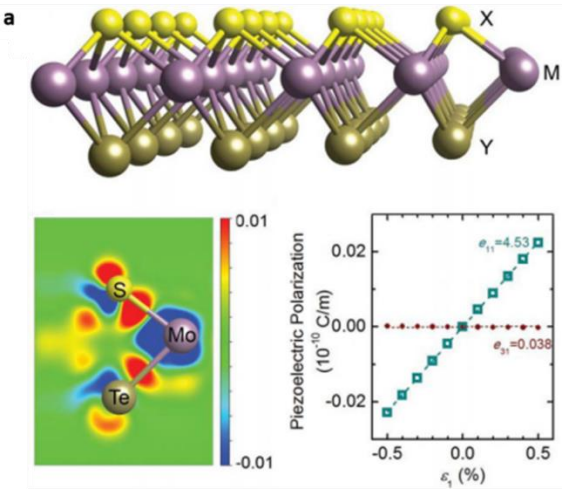

Fig 1. 12 Piezoelectricity with respect to strain in 2D Janus TMDc [83].

Studies of the in-plane and out-of-plane piezoelectric properties in SeMoS Janus revealed that strain could be used to boost the out-of-plane piezoelectric coefficient significantly. This can also be achieved by constructing a vertical Janus homojunction, where altering the stacking sequence can tune the piezoelectric property and even surpass

the piezoelectric coefficient of popular bulk piezoelectric materials. Janus heterojunctions have been in focus due to asymmetry-influenced interface variations and permanent dipoles within the layers [83]. According to the studies by Li *et al*., both vertical and lateral heterostructures of SeWS/SeMoS had a type-II band alignment. This arrangement induces spatially indirect excitons [87], making type-II band alignment Janus structures suitable for energy conversion applications. Riis-Jensen *et al*. report that the presence of intrinsic dipole moment results in the emergence of a built-in electric field [86]. When reaching a critical thickness of 3-4 layers, electron transfer occurs between extreme end layers. Due to such a band alignment the distance between CBM of the top layer and VBM of the bottom layer becomes minimum. A p-n junction created to test the charge density showed that it can be significantly tuned depending on the number of layers present in the Janus structure. Based on these results, application in solar cells for charge separation seem highly probable [83]. Zhou *et al.* has suggested that in a bilayer SeWS structure (Se-S-Se-S) there is a significant layer splitting due to the net dipole moment sensitive to the interlayer separation distance. This can again prove useful in solar cell devices [81].

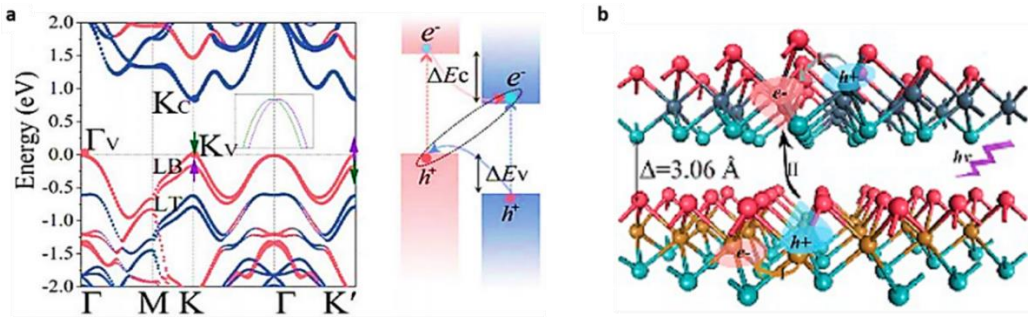

Fig 1. 13 a. Intrinsic polarization field cause type-II junctions to form in bilayer homojunction Janus structures [83]. b. Strong polarization fields form interlayer excitons in Janus SeMoS/SeWS heterojunctions [83].

More experiments reveal data on quantum properties arising from the many-body interactions and permanent polarization fields in Janus monolayers. Applications in Opto-spintronics, 2Dmagnetic knots, and qubit operations enabled by the colossal Rashba splitting and piezoelectric devices [83] will revolutionize the electronic industry as we see it now.

1.5.2. Janus synthesis review:

The first reports of group VI-based Janus material synthesis came from Lu *et al.* and Zhang *et al.* in 2017 [88][89]. However, even after these results were published, experimental studies on crystalline Janus properties remained elusive simply due to the challenges faced in sample preparation, synthesis, and quality of the material thus synthesized.

In 2017, Lu *et al.* reported Mo-based Janus materials synthesis. Lu *et al.* started by stripping the sulfur atoms on the top layer of the MoS_2 monolayer using hydrogen plasma. The etching was followed by thermal selenization of the intermediate MoSH structure at 350ºC – 450 ºC, forming the SeMoS Janus structure [89]. Zhang *et al.* reported the synthesis of SeMoS structure through controlled sulfurization of monolayer $MoSe_2$ in a typical CVD setup [88]. Their process involved heating a $MoSe_2$ monolayer in a CVD setup at 800ºC. The heated sulfur powder, used as a chalcogen source, was transported to the monolayer surface through ultra-pure Argon gas. At very high temperatures, the thermal driving forces help sulfur to replace selenium by overcoming

the thermal barrier, resulting in the formation of the Janus structure [88]. However, the PL line width of the Janus structure was broad. These results indicated that the process resulted in many defect formations due to the high processing temperatures.

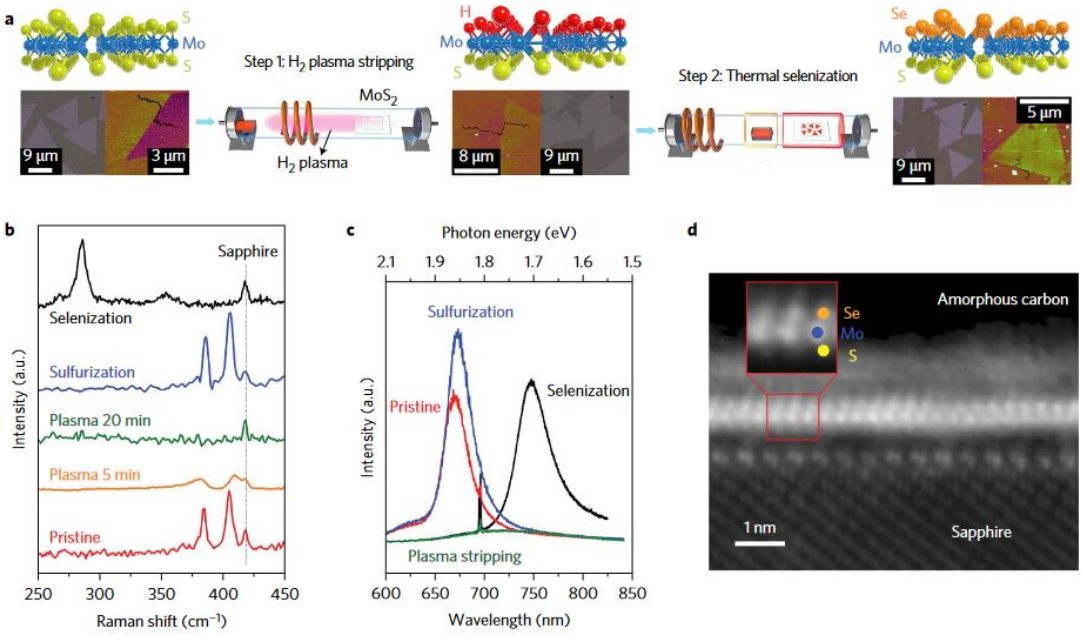

Fig 1. 14 a. Schematic showing steps followed in the synthesis process for SeMoS structure b. Raman spectrum comparing pristine, intermediate, sulfurized, and selenized TMDc structures. c. PL spectra for MoS_2 pristine, selenized, and sulfurized to restore MoS_2. d. Cross-sectional TEM showing SeMoS Janus monolayer structure [89].

To synthesize Janus materials exhibiting better optical behavior, a radically new method, termed selective epitaxy atomic replacement (SEAR), was developed. SEAR relied on the generation of hydrogen radicals through the inductively coupled plasma at room temperature for etching and replacement of exclusively top layer chalcogen atoms [74]. Utilizing the SEAR method, Trivedi et al. published results for the synthesis of Janus SWSe monolayers as well as W and Mo-based Janus heterostructures

(SMoSe/SWSe) [74]. Furthermore, Janus crystals synthesized via SEAR had a higher degree of crystallinity and relatively lower defect density, as evident from the sharp Raman spectra PL emission and FWHM [74] for SWSe and SMoSe.

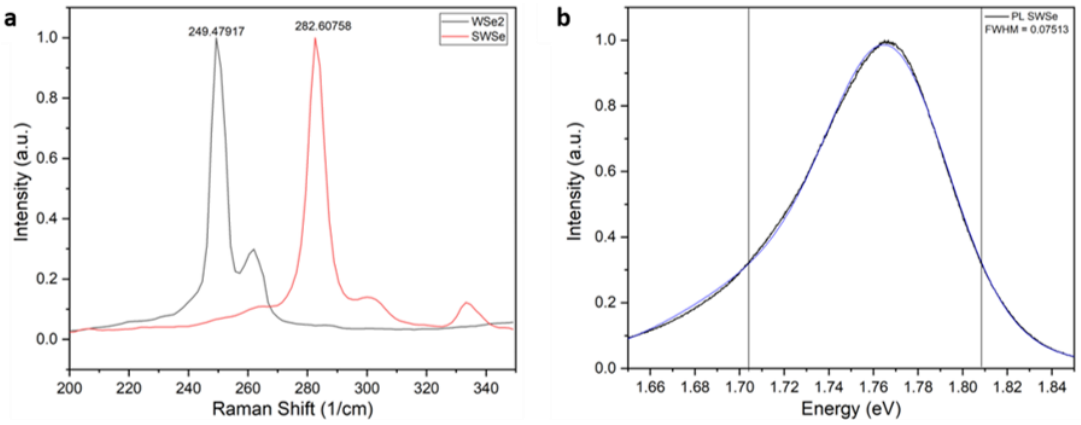

Fig 1. 15 a. Raman Spectra of monolayer WSe_2 (black) compared to SeWS (red). b. Photoluminescence spectra for SeWS Janus and FWHM.

Thus, the development of the SEAR technique offers immense potential to expand the Janus materials library and creates an opportunity for in-depth study of the emerging quantum properties in these materials.

Chapter 2 : Synthesis and Characterization Techniques

The foremost aspect of performing experimental studies and collecting real-time data is successfully synthesizing the required material system. Synthesis of a crystalline structure is essential to study the newly emerging optical, electronic and structural properties brought by Janus materials. There have been some successful attempts in the recent past to synthesize this new class of materials, but very few have been able to replicate those. Due to the existence of thermodynamically favorable MXY alloys, it becomes paramount to have precise control over the atomic replacement of one chalcogen with another. This is essential to avoid alloying and obtain a highly crystalline Janus material consecutively. This section will focus on some tools and techniques essential for the growth and characterization of TMDc Janus materials.

2.1. Chemical Vapor Transport (CVT)

Chemical Vapor Transport reactions are used to synthesize high-quality crystalline solids, especially for the production of single-crystalline bulk material. The process involves chemical reactions based on thermodynamics, the stoichiometry of solid precursors, and transport agents. In this process, solid precursors are loaded in a quartz ampoule which is then sealed under a pressure of 10^{-5} Torr to avoid contamination from atmospheric gases [90]. These precursors are loaded at one end of the ampoule and then placed in a furnace to heat the precursors. The reactions usually occur at very high temperatures at which solid precursors sublimate and are transported with the help of a

transport agent [90]. As a result, the crystals form in the relatively colder zone of the ampoule. The factors which play a critical role in the synthesis of high-quality single-crystalline structures include but are not limited to the stoichiometry of precursors involved, reaction temperature gradient, and transport agent. These reactions depend extensively on the kinetics and thermodynamics of the reactants involved in the growth process. For most vapor transport reactions, elemental precursors are used as the charges, but in some cases, the vapor pressure of precursors might not reach the required level for the transport mechanism to occur. Thus, transport agents (elemental halides) are mixed with the precursors to facilitate the transport mechanism. Halides reversibly react with metal at high temperatures, forming metal halides with a low melting point and high chemical potential [91]. After reaching thermo-equilibrium and forming a stable phase, the halide leaves the product and transports more precursors to the targeted zone.

For the synthesis of Tungsten diselenides, elements in their powder or granular form are sealed in a glass ampoule under a secondary vacuum ~ 10^{-5} torr. For growth, the temperature was set to reach 1050 ºC in 48 hours. The ramp rate was set at 21.35 ºC/hour so as to avoid any risk of ampoule explosion due to fast pressure buildup by selenium vaporization. Once this system reached desired temperatures, it was kept under these conditions for 96 hours. Then it was programmed to reach 750 ºC in 72 hours and naturally cool down to room temperature afterward.

Fig 2. 1 WSe_2 bulk crystal-synthesized via chemical vapor transport © 2D semiconductors.

Synthesis of a bulk Janus structure with unique atomic layers and exact ratio of the atoms of materials systems is still limited by the current growth technology and techniques. The reactions in a CVT synthesis occur at very high temperatures where the kinetic energies of the individual atoms are too high for controlled growth to happen on individual planes. Thus, it is more probable to find the growth of a randomized structure showing two different phases as it is more energetically favorable.

2.2. Mechanical Exfoliation

The TMDc vdW bulk crystals produced via CVT reactions can be exfoliated into monolayers, followed by alteration of the atomic structure of the crystals to create a Janus structure. Exfoliation and transfer remain among the most accessible and successful techniques to obtain high-quality single or few-layer nanocrystals from their original multi-layer structures. In the scope of this thesis, mechanical exfoliation of bulk crystals such as Molybdenum Selenide and Niobium selenide was undertaken to obtain their

monolayer equivalent. The exfoliation process can be carried out in various ways, such as liquid-assisted, chemical, and mechanical exfoliation (metal-assisted and scotch tape-assisted). Mechanical exfoliation has become a popular method for isolating monolayers from a highly crystalline vdW bulk TMDc crystal. These materials can be exfoliated to the monolayer limit because of the weak vdW interaction between two layers and low out-of-plane cleave energy.

The adhesion between the substrate and the monolayer should be stronger than the vdW interaction between the layers of the material. Polydimethylsiloxane (PDMS) has also been tested to improve the probability of obtaining a monolayer. The use of PDMS decreases the adhesive residue left on the substrate surface and enhances the yield of monolayers. As the layer of PDMS is peeled off the substrate, the vdW forces from the substrate and the adhesion from PDMS tear the crystal in opposing directions, resulting in the cleavage of the bulk crystal into a few layers, bilayer and monolayers that stick on top of the substrate via vdW interaction [92]. Treating the substrate with O_2 plasma before exfoliation improves the reactivity of the substrate by removing the organic contaminants from the surface. In Fig 2.2, all the steps for mechanical exfoliation have been shown in sequence; (1) Bulk crystal is exfoliated on a scotch tape by repeated pasting and peeling of original tape onto new ones until the desired thickness of crystals is achieved. (2) Pasting the PDMS layer on the tape containing the crystals. (3) Peeling the PDMS piece from the tape to get thin crystals. (4) Stamping PDMS on top of Si/SiO_2 substrate for transferring crystals on the substrate. This process results in the transfer of thin crystals onto the substrate.

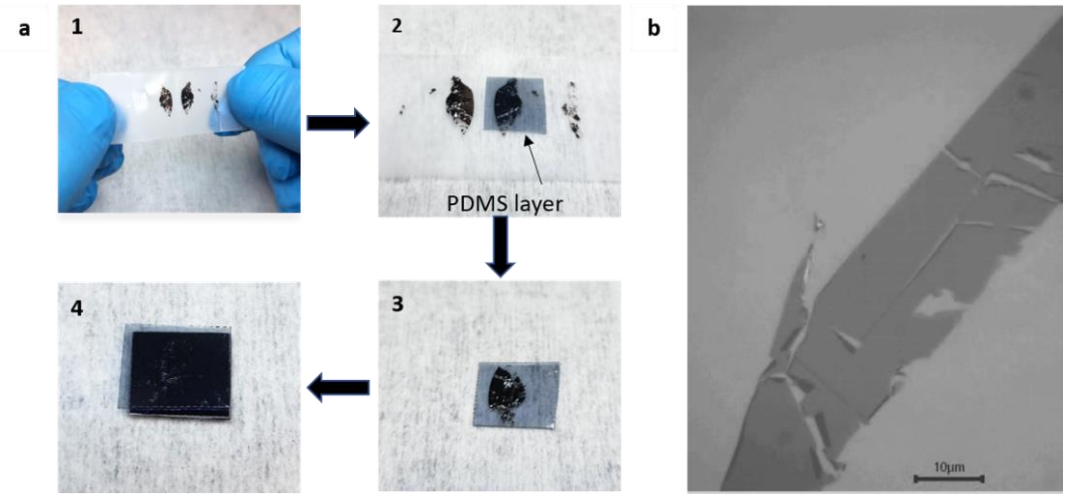

Fig 2. 2 a. Process of scotch tape exfoliation b. Optical image of mechanically exfoliated WSe_2 monolayer on Si/SiO_2 substrate.

2.3. Chemical Vapor Deposition (CVD)

Among all the available synthesis methods, chemical vapor deposition is the most popular for growing 2D materials at a large scale. The CVD process relies upon gas-solid chemical reactions to produce 2D films. It is constrained by the laws of kinetics and thermodynamics of the gas phase reactants. CVD can be performed at high and low temperatures, where pressure can be maintained at atmospheric levels or reduced to a millitorr regime, depending on the desired composition, structure, and morphology of the required materials system.

In a typical Atmospheric Pressure CVD (APCVD) system, the reaction occurs at high temperatures inside a quartz tube supported by a tube furnace system. Precursors are placed in a ceramic boat, and the substrate is placed on top of the boat for minimum distance and higher deposition rates of the gaseous phase reactants. At set temperatures,

gaseous precursors are carried over the substrate by inert gases such as Argon or Nitrogen, and reactive gases such as H_2 are used as catalysts or facilitators for the reaction. As the chemical reactions take place on the substrate resulting in the deposition of monolayer/few-layer structures, byproducts are pumped out of the reaction tube with the help of a pump. Many factors need to be optimized in order to synthesize the desired: (i) morphology, (ii) thickness of the film, and (iii) size of the crystals, are but not limited to: (i) temperature at which reaction takes place (ii) gas flow rate (iii) stoichiometry of precursors (iv) cooling rate of the substrate once the reaction is over and also (v) sample preparation steps like improving substrate reactivity by various cleaning methods to make it more favorable for nucleation of crystals. Once these parameters are adjusted, large-sized monolayer crystals with high crystallinity can be mass-produced. In the setup shown in Fig 2.3 (a), MoO_3 powder and substrates are placed in the center of the reaction tube for the growth of $MoSe_2$ and MoS_2. The chalcogen source (Se/S) is located upstream, where the temperature is kept between 300 and 200 °C. $MoSe_2$ growth uses 24 sccm Ar and 4 sccm H_2, whereas MoS_2 growth uses 20 sccm Ar. The furnace is ramped at a rate of 30 °C/min to reach 760/700°C and held there for 10-20 minutes before naturally cooling it down to ambient temperature [93].

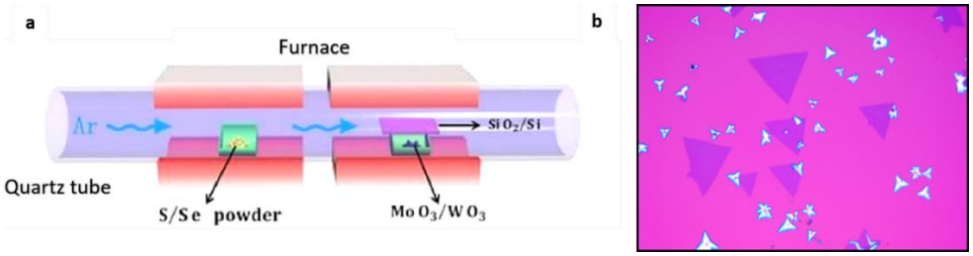

Fig 2. 3 a. Schematic for a simple CVD growth system. b. CVD grown $MoSe_2$ monolayers and few-layer crystals on Si/SiO_2 substrate.

2.4. Selective Epitaxy Atomic Replacement (SEAR)

Creating a stable 2D Janus structure is a complex process requiring a precise atomic level operation to achieve desired results. There are only a few routes available for synthesizing 2D Janus materials. Two of these methods involve etching the top layer of chalcogen at very high temperatures and subsequent replacement with other chalcogen atoms. The other route for conversion was attempted through low-energy ion implantation at 300ºC. These processes increase the chances of creating a highly defected Janus structure or thermodynamically favorable 2D alloy [74]. Due to the drawbacks of the methods mentioned above, our team synthesized Janus from TMDc through plasma-assisted atomic alteration, termed selective epitaxy atomic replacement (SEAR).

SEAR involves the use of plasma generated at room temperature through inductive coupling (ICP) to etch away the top chalcogen layer of a monolayer sample. ICP-based plasma is formed using an RF source and a helical copper coil wound on a dielectric chamber. In this case, a cylindrical quartz tube, generally used for CVD, filled with hydrogen gas was used for the reaction. When an electrical current changing with time passes through the coil, it generates a varying magnetic field around it [94]. The varying electromagnetic fields ionize the hydrogen gas inside the reaction chamber, which results in the formation of free electrons. These electrons get accelerated due to the influence of the fields and generate more charged species by colliding with freestanding atoms of the gas. This phenomenon initiates an electron avalanche that continues until a balanced degree of ionization is reached. Here the degree of ionization can be stated as follows:

$\alpha = n_i / (n_i + n_a)$; where [n_i = density of ions; n_a = density of neutral atoms]

The carrier gas can be ionized beyond the visible plasma glow or discharge tail. The strength of the plasma generated can be controlled by changing the RF power to the coil, which is one of the many crucial parameters required for a successful Janus conversion. Some other parameters besides RF power that influence the conversion process can be: (i) the pressure inside the reaction chamber during the process, (ii) gas flow rate, (iii) the position of the copper coil on the reaction chamber, (iv) relative position of the substrate with the replacement chalcogen source to the plasma tail end, and (v) processing time for the SEAR process. Depending on the binding energy of the transition metal with the chalcogen that needs to be replaced, parameters such as the RF and the processing time must be optimized accordingly.

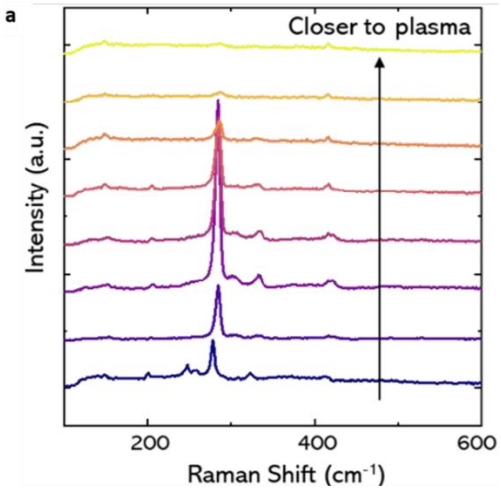

Fig 2. 4 Effect of distance from plasma tail on the Janus conversion efficiency of SEAR process [93].

Optimization of the position of the sample and chalcogen source is essential as placing the sample too close to the plasma tail end will lead to over-etching and other

structural damage like surface cracking due to the higher rate of reactive ion bombardment. An opposite effect is seen if the sample is placed very far from the plasma tail might result in very little to no etching due to the absence of enough reactive ions needed for uniform etching. The distance between the chalcogen source and the sample also has similar effects. Improper distance will result in inadequate and non-uniform replacement mechanisms.

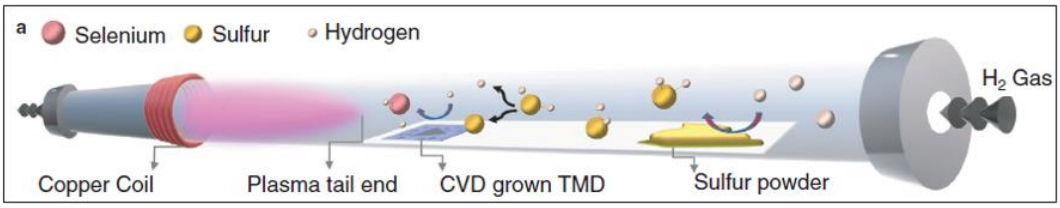

Fig 2. 5 Schematic representation of SEAR process conducted through Inductively coupled plasma [95].

With a modified chamber that allowed for in-situ monitoring via Raman spectrometer setup, it was possible to monitor the SEAR process from the starting of the etching process to the replacement by another chalcogen atom and the formation of the Janus structure. Monitoring Raman peaks of the parent TMDc throughout the process exposes the mechanism through which SEAR works. For better control of the as-synthesized Janus structure, some modifications in the design of the reaction chamber were done. The new reaction chamber also used ICP to generate reactive ions and radicals necessary for the Janus conversion mechanism, which has been discussed in the upcoming chapter.

The samples converted for preliminary studies were placed inside a 1-inch-wide quartz chamber, as shown in Fig 2.5, at a pressure maintained around ~ 300 mtorr, and

the tube was flushed with 20 sccm of high purity H_2 gas through a mass flow controller. Plasma was generated at 15-20 W RF power, at 13.6 MHz frequency, and the sample and sulfur source were placed in the plasma tail's optimum vicinity. The H_2 molecules dissociate into H free radicals and H^+ ions. H free radicals being very reactive species, bond with the top chalcogen layer and form intermediate species while the H^+ energetic ions bombard these intermediate bonds and form H_2Se/HSe^+ byproducts. This process results in chalcogen vacancy formation on the top layer [74].

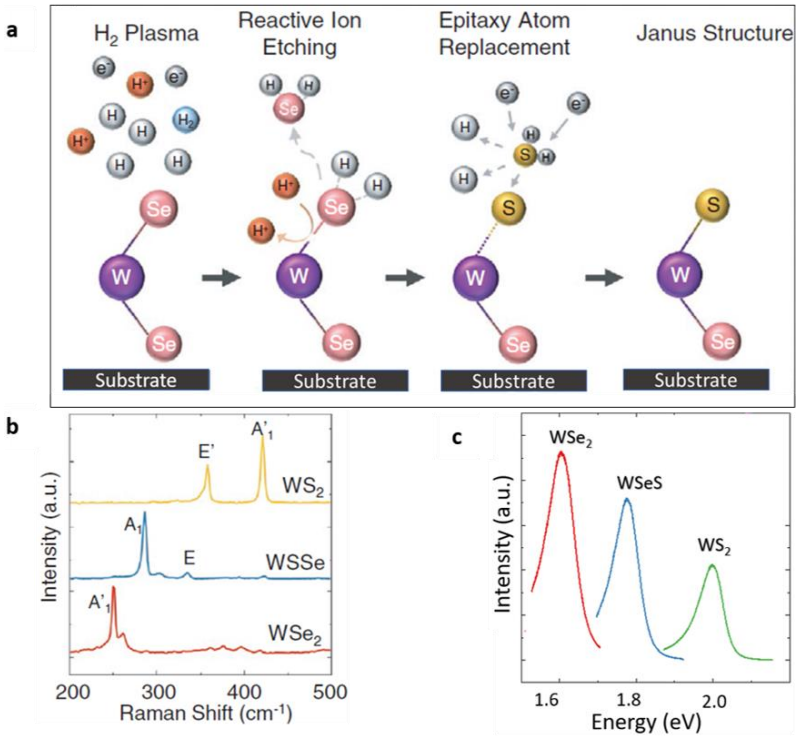

Fig 2. 6 a. Working mechanism of SEAR at room temperature. b. Raman spectra comparison of WSe_2, SeWS, and WS_2 with FWHM of most prominent peaks being 5.5, 5.1, and 4.4 cm^{-1}, respectively. c. Photoluminescence spectra of WSe_2, SeWS, and WS_2 with FWHM being 115, 92, and 80 meV, respectively [74].

The H_2S molecules formed over the sulfur source are transported to the sample with gas flow and dissociate into H and S species. The sulfur radicals get incorporated into the

chalcogen vacancies and form a stable Janus (SeMS (M = W, Mo)) structure. The etching of selenium atoms and replacement with sulfur atoms take place simultaneously. For synthesizing a highly crystalline Janus structure, a sufficient amount of chalcogen atoms in the form of H_2S or sulfur radicals should be present in the chamber throughout the reaction [74].

2.5. Pulsed Laser Deposition:

Pulsed laser deposition is a type of physical vapor deposition that uses a pulsed nanosecond laser beam to evaporate pellets of target material in a low-pressure, oxygen-containing atmosphere [96]. A nearly stoichiometric "plume" of that material is carried to a heated substrate under these circumstances, where the material nucleates to form well-controlled thin films, or layered structures of numerous films, with nanometer-scale accuracy[96]. This type of synthesis is used to investigate the effects of interfaces, confinement, and layer coupling. Complex metal-oxides with several atomic components are the most common materials [97].

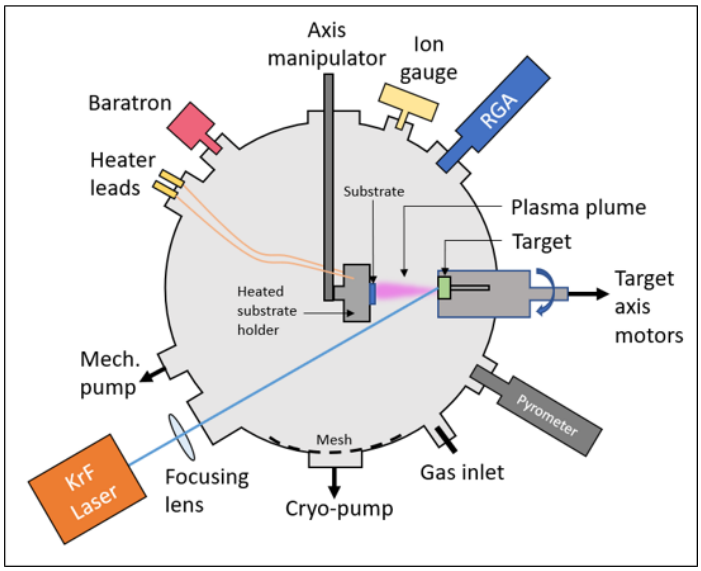

Fig 2. 7 Schematic showing low energy implantation process occurring in a PLD chamber, utilizing a KrF laser source [98].

In a PLD setup, a stainless-steel chamber is kept at a vacuum of about 10^{-8} torr. A manipulator with multiple targets can be used to form multi-layered structures, superlattices, or oxide-doped materials [97]. A pressure controller keeps the required (O_2/N_2/Ar) pressure in the chamber. Krypton fluoride (KrF) or argon fluoride (ArF) excimer lasers with wavelengths of 248 or 193 nm, respectively or Nd-YAG lasers with a wavelength of 355 nm, are generally used as energy sources [99]. Repetition rates of up to 50 Hz are common. Excimer lasers have the advantage of high-power output and stability [98]. A lens is placed in the path of the laser beam for focusing it onto the rotating or 2D-stepped target, controlled by a motor-driven manipulator. Usually, the angle of incidence of the beam at the target is 45-60°, and the laser spot size is around ~ 0.1 mm^2. The target-sample distance is adjustable up to 10 cm [99]. Inside the vacuum chamber, the pulsed laser beam is focused on a solid target that is to be deposited. The

target material is vaporized, ionized, and ejected as a plasma plume spreads towards the sample inside the deposition chamber [96]. After hundreds or thousands of laser pulses, the ablated species condense on the substrate opposite the target, forming a thin film. The plasma properties of the generated plume is the deciding factor when it comes to the quality of the deposited thin film [100].

Recently PLD has been used as a top-down synthesis method for compositionally altering monolayer TMDc to form Janus materials [98], [101]. Studies have been done showing how the hyperthermal nature of pulsed laser ablation plasma can be controlled to implant Se species with KE<10 eV/atom into WS_2 or MoS_2 monolayers [98], [101]. It has been indicated that by controlling the KE, selective and complete Selenization of the top layer of suspended or supported WS_2 monolayer can be achieved to form high-quality Janus SeWS ML at low (300-400°C) temperatures in an implantation and recrystallization process using PLD [98], [101].

2.6. Raman Spectroscopy

Raman Spectroscopy is a non-destructive technique used to analyze a material's vibrational, rotational and low-frequency modes. This technique provides detailed information about defect concentration, phase and morphology, crystallinity, and molecular interactions as the technique is based on the interaction of light with the chemical bonds within a material.

A highly coherent laser is used for exciting phonons above their ground state. The difference in the photon energy between the excitation and the scattered beam is absorbed

by the crystal in the form of vibrational energy and is obtained in the form of the Raman shift. This Raman shift can be defined as $Raman\ shift\ (cm^{-1}) = \frac{1}{\lambda_0(cm)} - \frac{1}{\lambda(cm)}$, where λ_0 and λ are photon energies of the incident and scattered beams, respectively. The basic setup of a Raman spectrometer consists of a light source such as a laser, a CCD detector, and an edge filter.

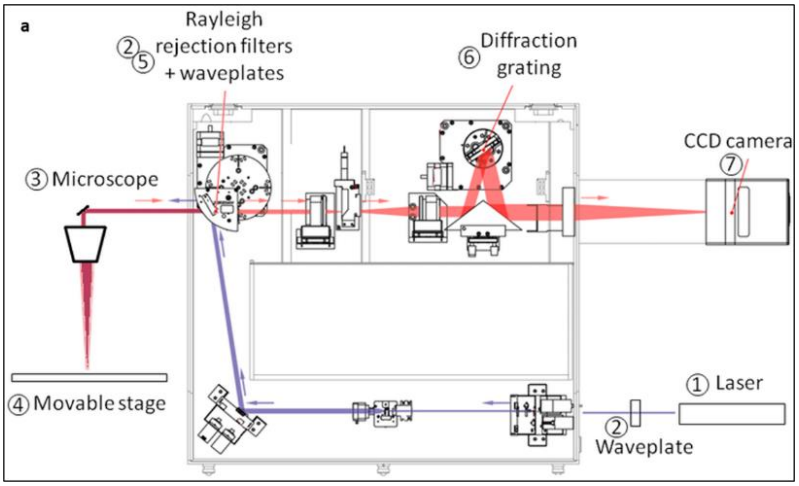

Fig 2. 8 Schematic representation of Raman Spectrometer © Renishaw

As shown in the schematic, the monochromatic laser produced by a laser source enters the system through the laser pinhole situated at the bottom right corner. Then, the laser is guided through a series of mirrors and filters, after which it is incident onto the sample, passing through a microscope objective. The phenomenon of the laser scattered inelastically by the phonons of the material system is known as the Raman effect. The scattered light retraces the same optical path and is detected by the photodetector, while the Rayleigh rejection filters filter the elastically scattered (Rayleigh scattering) light.

The non-elastically scattered light from the sample consists of stoke and anti-stokes scattered rays, determined by the type of interaction between photons of incoming light and phonons of the material system. At room temperature, the occurrence of the stokes shift is higher than the anti-stokes shift. This is because for the anti-stokes process to happen, phonons require a much higher amount of energy, which is barely available at room temperature, thus resulting in a lower occurrence rate. These Stoke and anti-Stokes processes are picked by the spectrometer, giving the peaks corresponding precisely to a wavenumber or frequency indicating a mode of vibration from the material's symmetry. These Raman modes can be compared to a theoretical phonon dispersion curve or fingerprint signals for a particular material system.

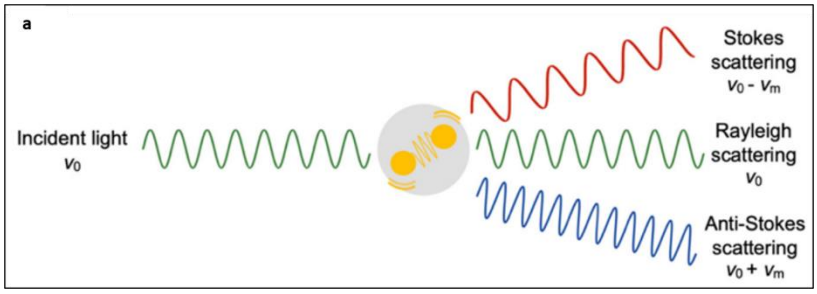

Fig 2. 9 Electromagnetic radiation interacting with a vibrating molecule revealing stoke, Rayleigh and anti-stokes scattering [102].

A minimal amount of backscattered light consisting of stokes and anti-stokes signals remains after the filtration. Thus, intensified CCDs are needed to collect relevant data to enhance the signal-to-noise ratio without extending the exposure to higher laser power. Long extended exposure to the laser can cause surface modification and may result in erroneous data collection. Therefore, measurements on sensitive samples should be

performed at lower laser power to avoid sample degradation. Increasing the number of signal accumulations per measurement is one way to improve the quality of collected data. The time of accumulation can also be increased to achieve the same effect.

2.7. Photoluminescence Spectroscopy (PL)

Another contactless non-destructive spectroscopy technique is Photoluminescence, which is used to probe the electronic structure of the materials, and uses the same instruments as of Raman Spectrometer. The technique uses the principle of photoexcitation which involves the generation of electron-hole pairs by the incident radiation of a specific wavelength. By providing the right amount of energy to electrons, they can be excited from the valence band to the conduction band. As electron combines with hole, it results in the release of energy. For a direct bandgap material, the electron-hole recombination process releases the photon with which the electron was initially excited. Now, if this process is a radiative process, meaning there is an emission of light, it is called Photoluminescence.

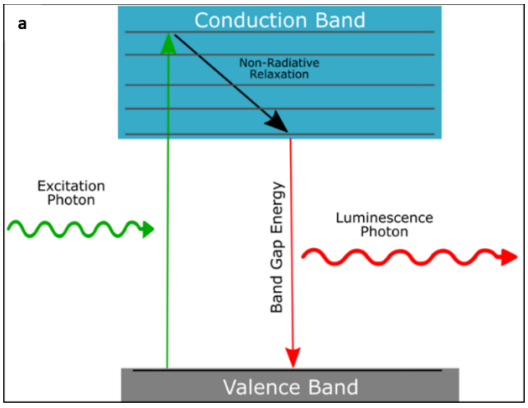

Fig 2. 10 Basic principle of Photoluminescence spectroscopy.

In the case of two-dimensional materials, due to the confinement of electrons and holes in one dimension, the electronic Coulombic forces between them increase, and an electron-hole pair is formed, termed excitons.

This process is critical for determining the band gap of electronic materials, studying the surface structure, and analyzing the surface recombination mechanisms and excited states. At room temperature, the energy of the emitted photon is either less than or equal to the material's bandgap. The optical bandgap for a material can be obtained from the interpretation of the plot of the intensity of PL emission vs. energy, where the energy value for a peak represents the optical bandgap. The optical quality of the material can be determined by calculating the Full Width at Half Max (FWHM) of a PL peak. The same can be done for estimating the relative concentration of defects for a material.

For measurements done at low sample temperature, the photoluminescence peak energy blue shifts following Varshni's Law [103]. According to Varshni's law, there is a change in the relative position of the valence and conduction band due to the temperature-dependent dilation of the lattice, thus affecting the electron lattice interaction, which decreases the bandgap of a material at low temperatures. This can be visualized through the empirical equation given by Varshni (eq.1)

$$E_g = E_0 - \alpha T^2/ (T + \beta) \qquad \text{(eq.1)}$$

Here, α and β are materials constant, E_0 is the bandgap at 0 K, and E_g is the bandgap at Temperature T Kelvin.

For indirect bandgap materials, the dominant recombination process is non-radiative type recombination, where heat is produced in this process assisted by the phonons instead of giving photoluminescence. In indirect bandgap materials, the recombination from VB to CB and vice-versa needs a phonon to help conserve the momentum. Thus, the characterization of indirect bandgap materials through PL spectroscopy is not a practical approach. While for direct bandgap materials, the optical bandgap can be easily extracted using the intensity Vs. Energy plot from PL spectroscopy.

2.8. Atomic Force Microscopy

One of the widely used techniques from the scanning force microscopy package is the Atomic Force Microscopy. It can be used to measure surface roughness, topography, and electric potential or to measure changes in physical properties arising due to atomic manipulation. For this measurement, a couple of micrometers long probe having a nanometer-sized tip is used to scan the surface quantitatively in X, Y, and Z directions with high precision at nanoscale resolution. The interaction between the tip and sample can also be used to alter some properties of the sample in a controlled and specific way, such as its use in scanning probe lithography.

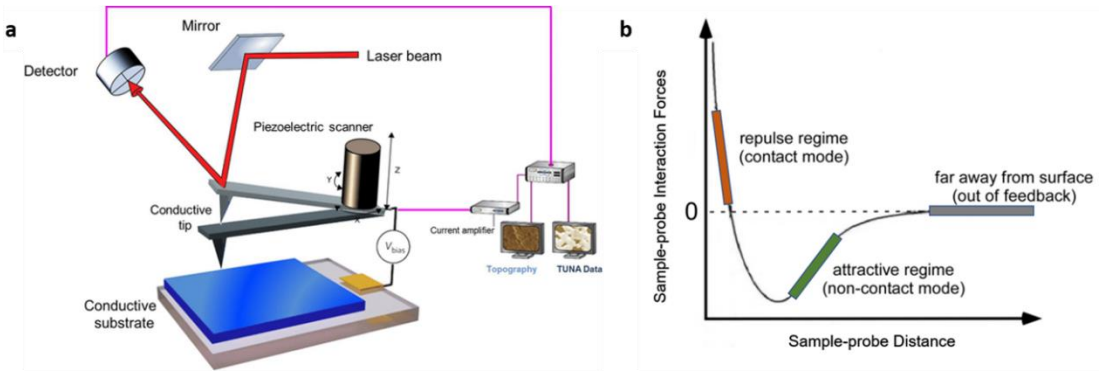

Fig 2. 11 Schematic showing how Atomic force microscopy works [104]. Sample-probe distance versus Sample-probe interaction force graph.

AFM working principle is based on the direct interaction of the cantilever (tip) assembly with the sample surface, ensuring a precise sample topography measurement. When the distance between sample and probe is of the orders of a few angstroms, due to overlapping electronic orbitals, the repulsive force is dominant. At this point, the sample and probe are said to be in contact. When the sample-probe distance increases, it causes polarization in atoms which causes attractive forces to dominate. Probes, also called cantilevers, can be made of different materials, usually silicon or silicon nitride, and come with a reflective or non-reflective coating. This ensures that different types of cantilevers can be used for specific applications. The tip scans the sample surface in a raster fashion, while the laser beam, which is reflected from the top of the cantilever, keeps track of the lateral and vertical motions of the tip throughout the scan. A position-sensitive photo detector (PSPD) monitors the changes in the laser beam and creates a high-resolution image of the scanned sample. The sample must be cleaned before the scan, as AFM scanning is very sensitive to contaminations such as dust or debris, and

common artifacts can be seen in the scans if the sample surface or the probe is contaminated.

2.9. Kelvin Probe Force Microscopy

Kelvin Probe Force Microscopy (KPFM) is one of the techniques available in the scanning probe microscopy pack, which is used to perform electrical characterizations such as mapping a sample's surface potential or work function. Work function can be defined as the amount of energy required to extract an electron from the Fermi level to a point in a vacuum that is very close to the outside surface of the sample. Work function is surface dependent property of a material rather than the bulk, which means that the information obtained by KPFM is either from the surface or near-surface region. There are two modes in which KPFM can operate, namely Amplitude modulation and frequency modulation mode. During this study, only the amplitude modulation mode of KPFM was used. Amplitude modulation is a dynamic force tapping mode in which an electrically conductive probe or cantilever is operated at its resonant frequency in one of the two setups that is single or dual-pass setup [105].

For the course of the experiments presented in this document, all the scans were taken in the dual-pass setup. In this setup, the cantilever scans twice over each line path as set in the scan parameter. For the second pass, the mechanism follows tapping mode, and the probe interacts with the sample to map out the topography, after which the tip is lifted at a height set by the user for the second-pass motion to take place. The lift-height parameter must be optimized so that the cantilever can be very close to the sample

surface, preventing the build-up of any stray capacitance between cantilever and sample, but also at a distance enough to not crash into the sample. As a result, the cantilever experiences mechanical oscillations due to the electrostatic forces generated because of the surface potential difference between the sample surface and the cantilever.

To nullify this potential difference and the oscillations produced in the cantilever, a DC value suggested by a potential feedback loop is applied, which is observed as the contact potential difference between the sample and cantilever. The double-pass scheme takes longer for image acquisition than the single-pass setup. Yet, it produces the best correlation between surface topography and surface potential scan due to the higher quality of spatial resolution generated.

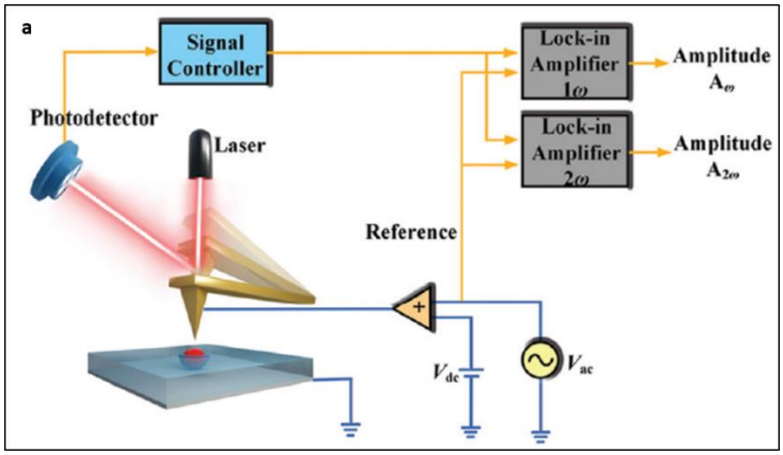

Fig 2. 12 Schematic representing KPFM block diagram [106].

A mathematical model is used to calculate a sample's local work function, which is based upon the contact potential difference (CPD) between the sample and the cantilever. Here, CPD can be expressed as:

$$V_{CPD} = \frac{\emptyset_{Probe} - \emptyset_{Sample}}{-e}$$

Fig 2. 13 Here, $\emptyset_{sample}$ and $\emptyset_{Probe}$ are the work functions of the sample and probe's tip.

Due to the difference in the Fermi level of the sample and the probe's tip, an electrical force is generated, which causes the probe to bend towards the sample surface. Fig 2.14 represents the schematic for the sample and probe energy levels. The vacuum energy level is represented by E_V, and the Fermi energy of sample and tip is shown as E_{fs} and $E_{ft,}$ respectively**.** At this point, the $\emptyset_{sample}$ and $\emptyset_{Tip}$ are at different levels. As shown in Fig 2.14 (a), the distance between the sample and the probe is extremely small, leading to electron tunneling from surface to probe or vice-versa. For this system to reach equilibrium, Fermi levels will align through the flow of electrons upon electrical contact between the probe and sample surface, which is shown in Fig 2.14 (b). At this point, a voltage difference forms between the charged sample and probe, representing the contact potential difference (V_{CPD}), also indicating that vacuum energy levels have also changed. Now the electrical forces acting on the contact area caused by V_{CPD} can be nullified. If an externally applied V_{DC} equals the $V_{CPD,}$ as shown in Fig 2.14 (c), the electrical forces or the surface charge can be entirely eliminated. Plugging the value of this measured V_{CPD} or its equivalent V_{DC} in the equitation from Fig 2.13 along with the $\emptyset_{Tip}$ will provide the value of the work function of a given sample.

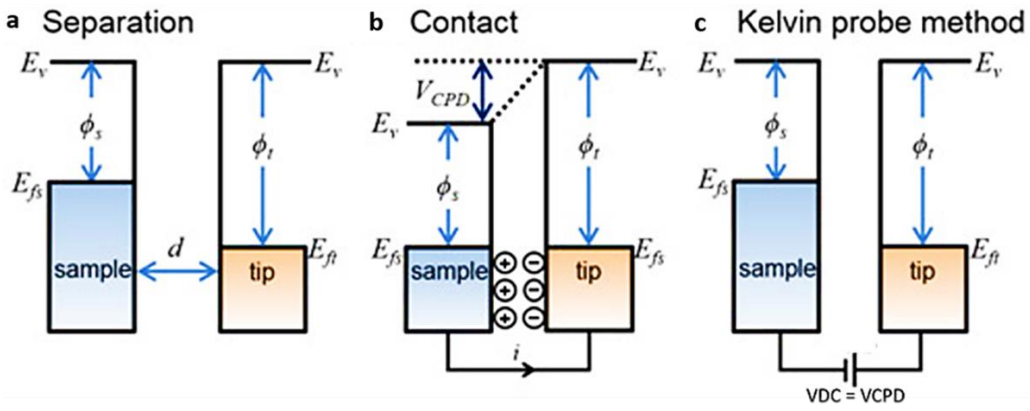

Fig 2. 14 **Electronic energy levels of the sample and AFM tip for three cases.**

Chapter 3: The microscale defects in Janus monolayers synthesized by selective epitaxy atomic replacement (SEAR)

Janus materials break out-of-plane symmetry and form a large polarization field, resulting in substantial Rashba splitting, and other quantum features worth noting[83]. Previous findings on the production of Janus materials, on the other hand, have relied on high-temperature processing, which invariably introduces defects into the final Janus structure[88]. In this chapter, we demonstrate the effective synthesis of highly crystalline Janus TMDc using the selective epitaxy atomic replacement (SEAR) approach at ambient temperature. We can convert CVT-grown TMDc monolayers in a two-step process using reactive ions and radicals produced in H2 plasma and an in-situ chalcogen source. We identify the structural, optical, and electrical properties of synthesized Janus monolayers and possible reasons for the effects caused by SEAR processing.

3.1. Synthesis of SWSe and SMoSe Janus monolayers

The synthesis of Janus monolayer starts with exfoliating bulk WSe_2 crystals grown by the chemical vapor transport process. Elemental pieces of Tungsten (Ultra-high purity 99.99%) were mixed with selenium pellets and $TeCl_4$ in a half-inch quartz ampoule. $TeCl_4$ has been proven to facilitate large-sized single crystal growth when used as a transport agent for growing TMDc materials via CVT [90]. The ampoule containing the mixture of transition metal, chalcogen, and transport agent was sealed under a vacuum of 10^{-5} torr. A three-zone furnace was used for the growth of bulk crystals where the temperature gradient between the hot and cold zone was equal to 20ºC. The precursor

side of the ampoule was placed in the hot zone (1050ºC), whereas deposition happened in the colder zone at 1030ºC. The temperature ramp rate was set at 21.35 ºC/hour. This moderately slow ramp rate was chosen to minimize the risk of explosion due to the sudden increase in vapor pressure of precursors inside the ampoule. After reaching the setpoint, the furnace was kept at 1050/1030 ºC for 96 hours. Afterward, it was programmed to gradually cool down to 750 ºC /730 ºC in 72 hours and then naturally cool down to room temperature. The whole process resulted in the formation of large crystals, up to 1 cm in size, with a high degree of crystallinity.

For the synthesis of bulk $MoSe_2$ crystals, a two-step, solid crystallization technique was followed. In the first step, the puratronic grade (99.99%), tungsten powder, and Se powder (99.99% purity) were mixed and sealed inside a quartz ampoule under a vacuum of 10^{-6} Torr. The powder mixture was heated and kept at 950 ºC for five days. In the second step, this pre-reacted powder mixture was resealed at (10^{-6} Torr) in a quartz ampoule with extra Se to achieve a 1:2 stoichiometry ratio and $TeCl_4$ powder. The trace amount of $TeCl_4$ was added to facilitate the formation of large crystals during the growth process. The ampoule was then kept in a three-zone furnace at 1080/1030 ºC (hot/cold zone) for 65 hours and then naturally cooled down to room temperature. The growth resulted in the synthesis of large-sized $MoSe_2$ bulk crystals.

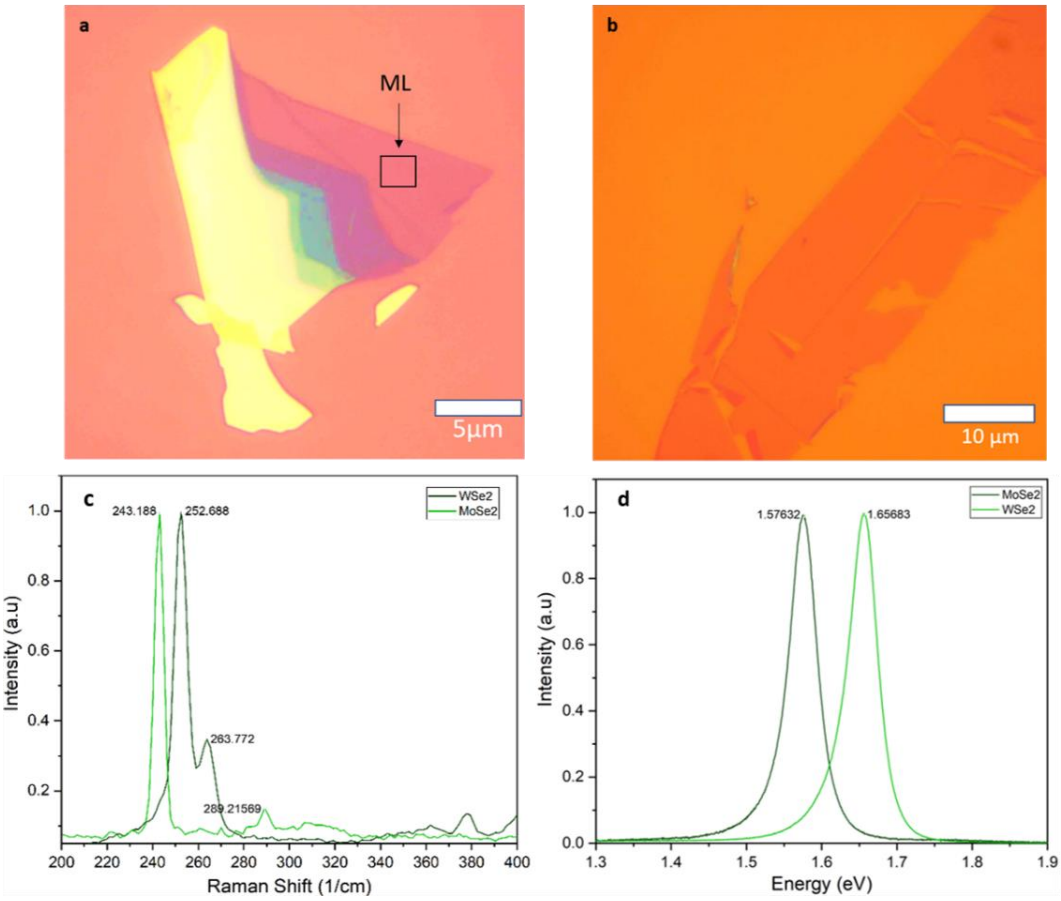

Fig 3. 1 a. Exfoliated $MoSe_2$ crystal on Si/SiO_2 substrate, monolayer shown (Black box). b. Exfoliated $MoSe_2$ crystal on Si/SiO_2 substrate. c. Raman spectra for $MoSe_2$ and WSe_2 taken with 488 nm (Blue) laser. d. PL spectra for $MoSe_2$ (FWHM = 45 meV) and WSe_2 (FWHM = 50 meV)

The Raman and PL spectra obtained for WSe_2 and $MoSe_2$ monolayers exfoliated from bulk CVT-grown crystals show narrow line widths of about ~3-4 cm^{-1} and 45-50 meV, respectively. These results confirm the high crystallinity for measured crystals obtained based on the CVT process. Moreover, the determined position of Raman modes (A_{1g} and $E_{2g}{}^1$) corresponds well with literature data for the studied here materials [57].

3.1.1. Preparation of WSe_2 and $MoSe_2$ monolayers from CVT-grown bulk crystals

TMDc crystals, such as WSe_2 and $MoSe_2$, are categorized as vdW materials that can be exfoliated using various techniques to obtain atomically thin layers [92]. Specific steps for sample preparation were followed to obtain sufficiently large monolayers of WSe_2 and $MoSe_2$. The first step was cleaning the substrates (Si/SiO_2) in ethanol, using the ultrasonicator for 5 min, and repeating the same process with isopropyl alcohol. The previous step is followed by blow-drying the wet substrates with ultra-high purity (UHP) nitrogen [92]. Finally, the dried substrates were subjected to oxygen plasma cleaning at 75W power for 15 minutes. The plasma cleaning process improves surface reactivity by eliminating any remaining organic impurities from the top surface of the substrate. The mentioned Si/SiO_2 wafer was used as a substrate for all the performed experiments, as it provides excellent optical contrast for the initial identification of monolayer and few-layer areas while observing under an optical microscope.

For thinning down bulk crystals to monolayer and few-layer form, the regular scotch tape was mainly used. The exfoliation procedure starts with placing a bulk crystal on a scotch tape and thinning it down with other pieces of tape until obtaining adequately thin and flat crystals. Next, the transfer of crystals from scotch tape onto a substrate was aided by a piece of polydimethylsiloxane (PDMS) sheet. The PDMS was placed over the chosen piece of scotch tape, peeled off, and then stamped over Si/SiO_2. As the last step, the PDMS was gently pressed to facilitate the transfer of crystals onto the substrate and removed. This process transfers large-area monolayers ($\geq 300\ \mu m^2$) alongside other few-layer and bulk crystals of different sizes.

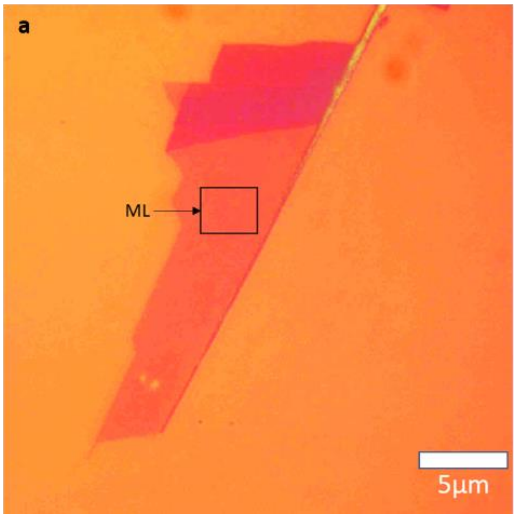

Fig 3. 2 a. Optical image of exfoliated WSe_2 monolayer (square box) crystal on Si/SiO_2.

3.2. Janus conversion of monolayer crystals

The conversion of exfoliated monolayers from CVT-grown WSe_2 and $MoSe_2$ crystals to Janus (SeWS/SeMoS) structure was performed using the newly customized SEAR chamber (Fig 3.3). Studies done within the scope of this work were preceded by optimization of the chamber to assure repeatability of the conversion process and exclude unwanted phenomena like the formation of alloy instead of Janus structure.

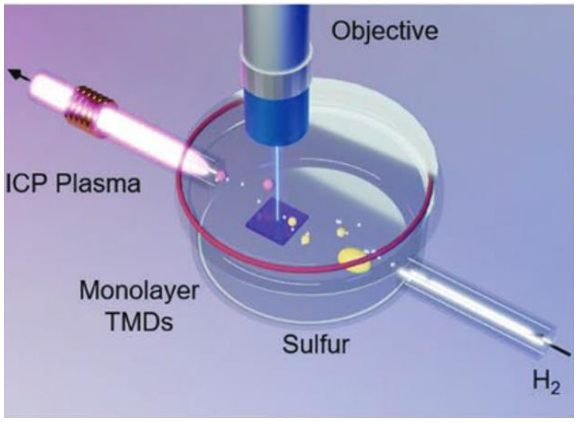

Fig 3. 3 Schematic for the latest version of selective epitaxy atomic replacement reaction chamber [95]

The schematic in Fig 3.3 shows the modified design of the Janus chamber, allowing for a constant gas flow over a sample. The flow rate of hydrogen gas entering the chamber is regulated by a 500 sccm mass flow controller, while a pressure gauge mounted on the gas outlet side of the chamber monitors the pressure inside. The unique design of this chamber allows for the collection of Raman and PL signals in-situ [93]. Monitoring time-dependent Raman spectra gives insight into the etching and replacement dynamics during the SEAR process. As the etching process starts, the intensity of the parent TMDc crystal Raman modes diminishes, and new modes corresponding to the Janus structure emerge [95]. The in-situ capabilities enable precise control of the conversion stage and avoid partial conversion or too long exposure to plasma. Thus with that approach, Janus conversion can synthesize structures of high quality [93][95][107].

3.2.1. Studying surface morphology of SWSe and SMoSe Janus monolayers

In the previous studies on Janus conversion of CVD-grown $MoSe_2$ monolayer, it was observed that the etching process during SEAR could result in surface crack formation [107]. For Janus samples synthesized based on exfoliated monolayers, the same features resembling cracks were observed through optical microscopy, as shown in Fig 3.4.

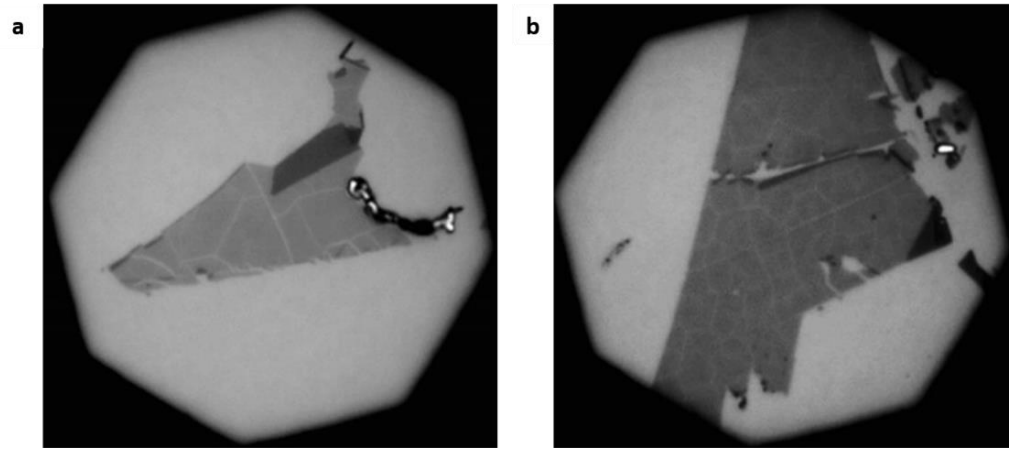

Fig 3. 4 a. Optical microscopy image of cracks developed in SeMoS monolayer post SEAR process. b. SeWS exhibiting surface cracks post-Janus conversion.

For detailed studies of the crack formations in Janus monolayers, measurements of as-synthesized SeWS films by atomic force microscopy were performed on NT-MDT atomic force microscopy setup in tapping mode. The sample was raster-scanned at 512-pixel/line at a 0.3 Hz scanning rate.

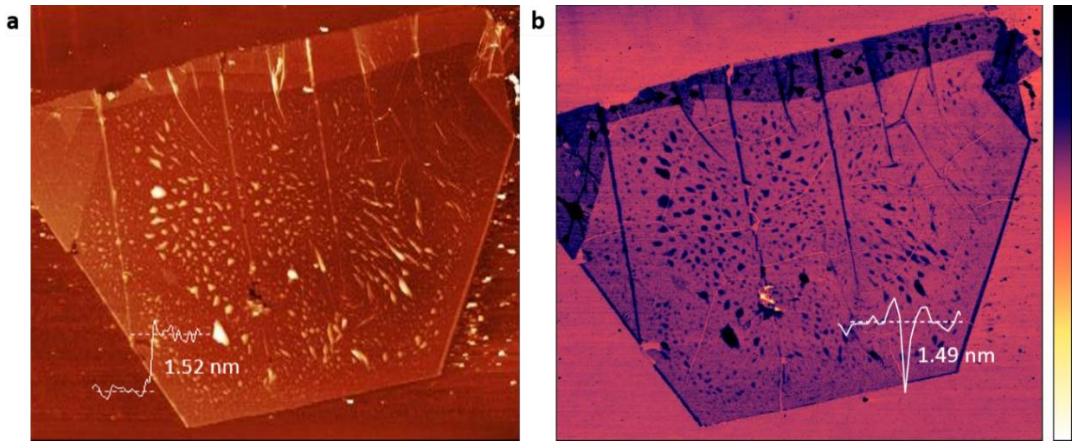

Fig 3. 5. a. AFM topography scan of WSe_2 monolayer before SEAR processing. b. Topography scan post-SEAR processing.

Topography image of the WSe_2 monolayer before Janus conversion shows no cracking features Fig. 3.5 (a). In contrast, the SeWS sample has developed cracks throughout the monolayer, as shown by the topography scan taken for the same area after SEAR processing. The observed cracks measure ~ 0.9–1 nm in depth and 3–5 nm in lateral size, as shown in Fig 3.5 (b). Here, we propose that the cracks observed in the Janus monolayer start propagating from vacancy defect lines. Such behavior was previously observed for CVD-grown monolayers exposed to hydrogen plasma treatment. As shown by the STEM image, sulfur vacancies were generated preferentially along the zig-zag direction of the crystal [108]. Since the SEAR process is also based on hydrogen treatment and driven by the etching dynamics, we expect that during the substitution process of chalcogen atoms, created vacancies will cause the formation of cracks. Utilizing the SEAR process for $MoSe_2$ leads to the formation of the same cracking features as seen in the SeWS monolayer Fig. 3.6.

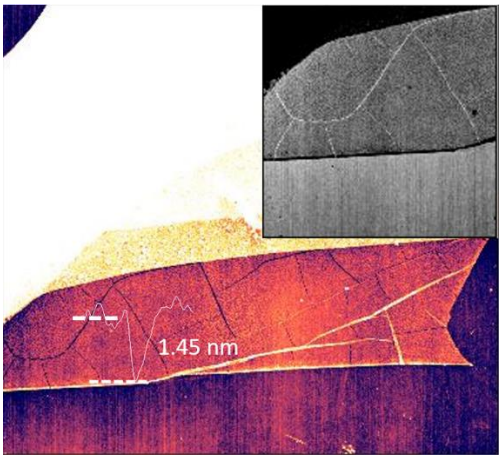

Fig 3. 6 AFM scan of SeMoS monolayer displaying surface cracks.

3.2.2. Fundamental understanding of surface cracking phenomena

It was shown that in CVD-grown monolayers, the different types of treatment, such as exposure to plasma or thermal annealing, can cause cracking [109], [110]. The formation of cracks usually is initiated at existing grain boundaries [110]. Since mechanically exfoliated monolayers from CVT-grown bulk are single crystalline in nature, cracks are formed differently (as it was briefly described in the previous chapter 3.3.1). In our studies, cracking happens as the result of sample exposure to hydrogen plasma during the SEAR process.

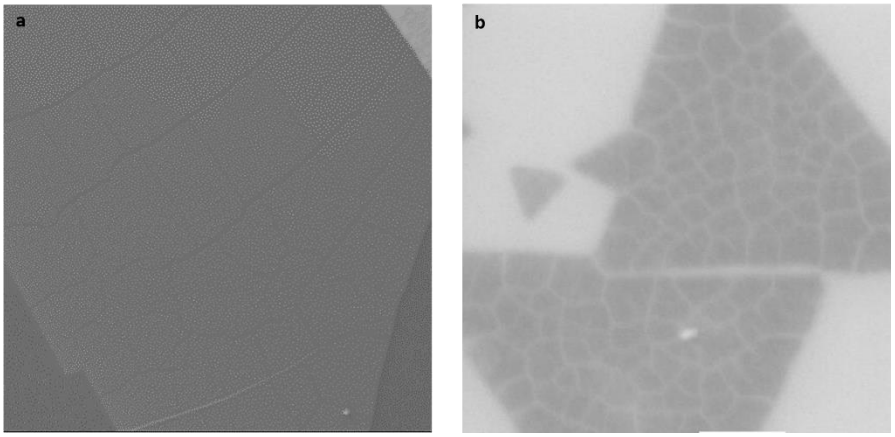

Fig 3. 7 SEM images of crack formation on Janus monolayers. a. SeWS Janus monolayer synthesized from CVT grown WSe_2 crystals. b. SeMoS Janus crystals produced from CVD-grown $MoSe_2$ crystals

It was proposed that the alignment of chalcogen vacancies formed during plasma etching is an intermediate step between crack formation and its propagation [108], [109]. Initially, the chalcogen vacancies are generated randomly, but as etching proceeds, the V_{Se} defects start to follow a zig-zag direction while aggregating. When ~50 % of the top layer selenium atoms are etched away, the monolayer cannot sustain the induced strain,

and crack formation occurs [108]. Since cracks start to propagate along the zig-zag direction, areas enclosed by them may resemble a hexagonal shape (interior angles of cracked islands = 120°). Thus we suggest that V_{Se} defect-induced strain has been the primary cause of crack formation in plasma-processed Janus monolayers.

During the SEAR process, as the TMDc monolayer (WSe_2) was subjected to the two-step process of etching followed by replacement with another chalcogen, the monolayer goes through stages of straining and relaxation. During the initial stages of the conversion process, there is no visible change in the Raman spectra. As the etching is happening and more chalcogen vacancies (V_{Se}) are created monolayer is subjected to increasingly larger strain. This behavior is evident from the shift of the A_{1g} mode from 250 to 261 cm^{-1}. At this stage, the in-plane strain caused by the V_{Se} formation is dominant throughout the material, and that can initiate the formation of cracks. Based on the Janus A_1^1 Raman peak shift from 285 cm^{-1} to ~282 cm^{-1} with time as conversion proceeded, it was concluded that the monolayer underwent relaxation. In Fig 3.8, at time (T1) the Raman spectra of WSe_2 monolayer is visible, around (T2) the A_{1g} mode of WSe_2 diminishes and near (T3) A_1^1 Raman mode for SeWS Janus starts to emerge. At (T4) only high intensity Janus SeWS Raman peak remains.

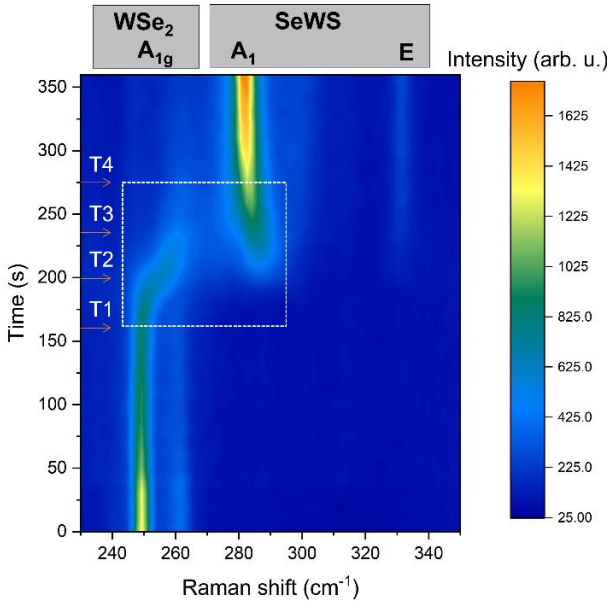

Fig 3. 8 Time-dependent Raman spectroscopy measurement for Janus conversion.

The V_{Se} defects formation during the etching process may act as a trigger for the formation of cracks since not all vacancy sites will be immediately replaced with another chalcogen atom. Subsequent propagation of cracks can follow zig zag or armchair direction. Based on the previous studies [108] and our findings, we have concluded that cracks form at the straining stage and propagate when relaxation occurs.

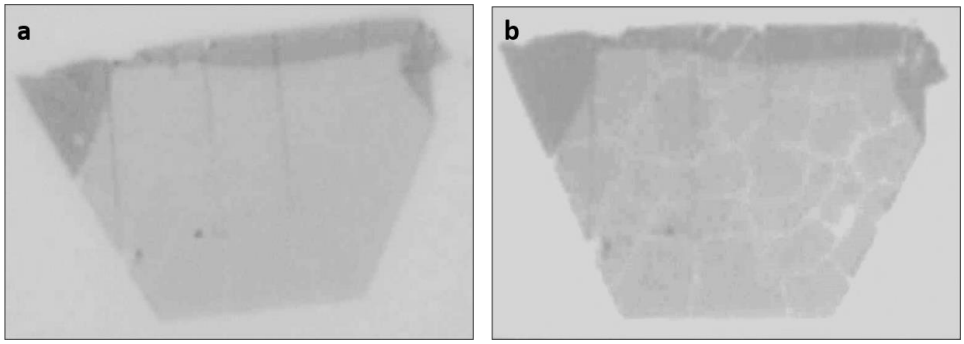

Fig 3. 9 Optical image for a. WSe_2 and b. SeWS monolayer (post-SEAR), showing monolayer-island formation due to crack propagation.

3.2.3. Optical properties of SeWS Janus monolayers

To study the optical behavior of as-synthesized Janus crystals, Raman and PL spectra were collected for a SeWS Janus monolayer with a 100x objective. The typical Raman spectrum for Janus materials differs from parent TMDc and WSSe alloy, which has randomly distributed sulfur and selenium atoms on both the top and bottom layer. For SeWS, the Raman spectra display four modes, among which the two most intense are located at 284 cm^{-1} and 331 cm^{-1} which are related to A_1^1 and E^2 modes, respectively [111]. The narrow linewidth of Raman modes (4 – 5 cm^{-1}) emphasizes the high crystallinity of synthesized SeWS monolayers. Furthermore, maps of Raman peak position and intensity of A_1^1 mode (284 cm^{-1}) Fig. 3.10 show that the replacement of selenium by sulfur has been almost homogenous throughout the monolayer area. The cracking pattern revealed by AFM imaging can also be seen in the Raman maps. The intensity of Raman peaks at the cracks is lower (200-250 counts) compared to the intact monolayer parts since the area of material from which signal is collected is reduced.

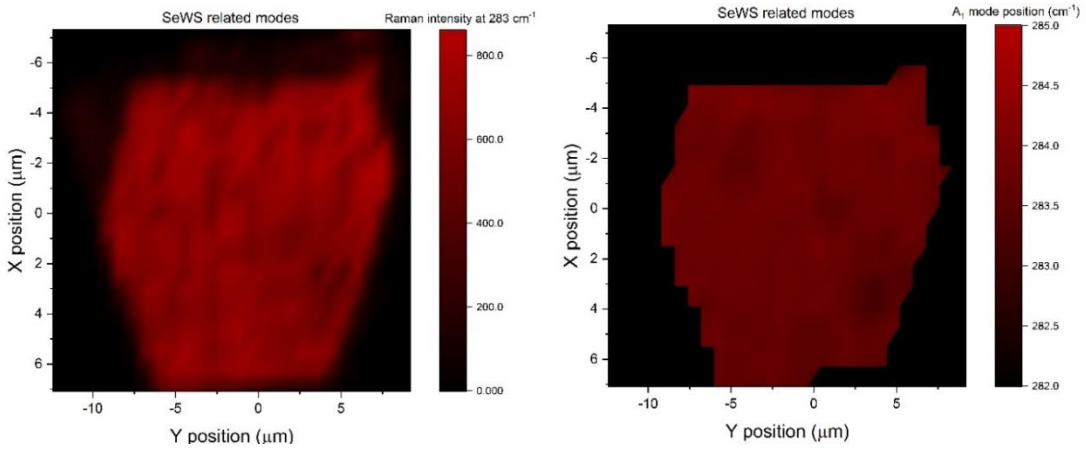

Fig 3. 10 a. Raman intensity map at 283 cm^{-1} positions (A_1 mode) for SeWS monolayer and b. map of the position of A_1 mode.

The emission peak from Janus SeWS is located at around 1.81 eV, potentially corresponding to neutral exciton recombination [95], where its line width was determined to be ~50 – 60 meV. The obtained maps of the PL peak position and its intensity shown in fig 3.11 indicate minor variations of these two parameters in some areas. This behavior can be related to two factors: (i) built-in strain and (ii) variation of Janus conversion stage, which, based on Raman measurements, can vary from 95 to 98 %. However, as mentioned based on Raman studies, overall conversion seems to be nearly consistent across the monolayer. There are only a few areas (Fig 3.11 (b)) for which the PL peak position shifts to lower energies ~1.75 – 1.77 eV. This might indicate a stronger defect contribution or different strain since the Raman map position of the A_1 mode shows its lower position in these areas.

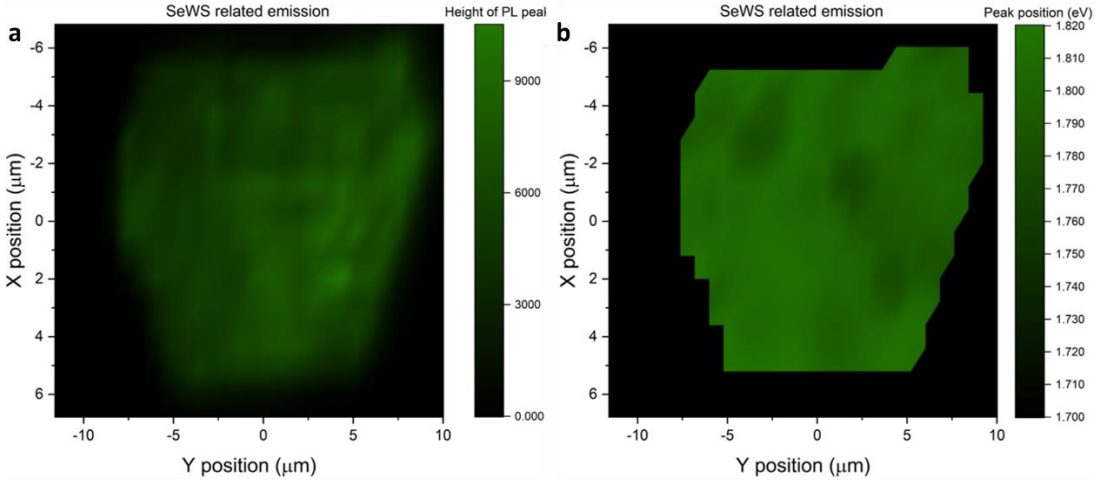

Fig 3. 11 PL intensity map at 1.81 eV (neutral exciton) for SeWS monolayer and b. map of the position of the neutral exciton (X_0).

3.3. Investigation of work function for Janus monolayers

Janus synthesis by the SEAR process involves several factors that must be considered to achieve good replacement efficiency of top chalcogen atoms. Wrongly selected parameters like, e.g., plasma power, time of the process, or sample position may lead to synthesizing a Janus structure: (a) not fully converted, (b) showing alloying behavior, or (c) with an excess of defects. We have proposed to use the surface potential quantity obtained by the KPFM technique to assess the conversion stage of the as-synthesized Janus monolayer. Based on this measurement, we have attempted to determine which areas of the monolayer were uniformly converted and whether some parts of the crystal still display properties characteristic of the parent TMDc material.

KPFM is a non-destructive microscopic technique that utilizes similar operating principles as AFM. Here, an AC bias was provided to the substrate, and the probe's tip scanned the Janus monolayer and registered the potential difference between the sample and the tip. This potential difference was nulled by supplying a DC voltage, thus generating a contact potential difference (CPD). From the measured surface potential difference across SeWS monolayer, its work function was obtained by subtracting the CPD values from the work function of the probe's tip. The work function for the probe tip was obtained by performing a KPFM scan for the HOPG thin crystals.

3.3.1. Surface potential measurement of Janus monolayers by kelvin probe force microscopy

The KPFM scan was performed using an NT-MDT Atomic Force Microscopy setup in Second (II) pass AM-SKM tapping mode. FMV-PT probe with Pt-Ir coating, designed

for electrical measurements, was used. Janus monolayer on a Si/SiO_2 substrate was raster-scanned with 512-pixel density at a scanning rate of 0.3 Hz. The AC biasing provided to the tip was 1 V, while the DC feedback value was modulated accordingly for each sample to offset the contact potential difference to zero. In the first step the work function of the scanning probe's tip was calculated by performing KPFM on HOPG (ZYA grade) flake on Si/SiO_2 (standard work function of HOPG in air = 4.5 eV [112]). From the surface potential plot of HOPG, the work function for the probe's tip was found to be 5.39 ± 0.02 eV. HOPG scans were performed before and after each measurement on Janus monolayers to check if the work function of the probe's tip was changing. This approach showed that the work function for the tip remained within the margin of error for 8 - 10 scans per probe.

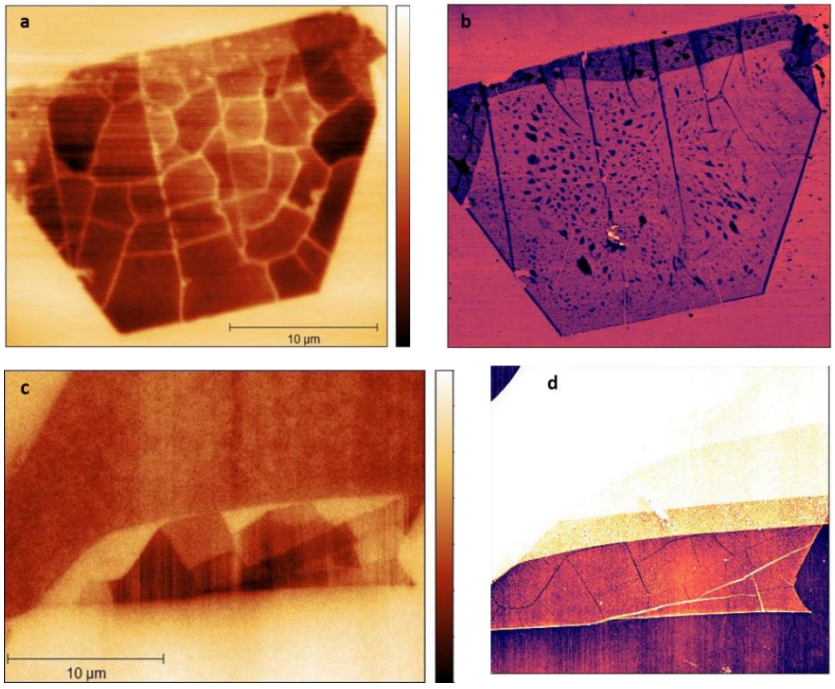

Fig 3. 12 a. Surface potential scan of SeWS Janus monolayer, b. corresponding AFM topography scan showing cracks. c. Surface potential scan of SeMoS Janus monolayer, and d. corresponding AFM topography scan of cracks.

The phenomena of crack formation in Janus monolayer of SeWS and SeMoS were identified initially by AFM measurements. Through the surface potential maps obtained by KPFM, we could observe the formation of multiple domains within a monolayer. Since the work function within areas enclosed by cracks is uniform and different from other such types of domains, we have named the observed behavior as a mosaic pattern.

3.3.2. Study of changes in work function between domains within a monolayer

Theoretically calculated (by Ph.D. student Taylan, within the DFT framework with PBE functional and including spin-orbit coupling), work functions for SeWS and SeMoS are in good agreement with experimentally determined values for these materials. Moreover, the work function for parent TMDc material also shows a good resemblance when comparing experimentally and theoretically obtained values. In addition, the surface potential detected across the Janus monolayer changes between domains, as shown in fig 3.12 (a, c). The work function values obtained were calculated using the equation $Ø_{Sample} = Ø_{Tip} - V_{CPD}$, where V_{CPD} was determined from the surface potential plot.

Material	Theoretical Ø sample (eV)	Experimentally observed Ø sample (eV)
$MoSe_2$	4.561	4.551
WSe_2	4.225	4.25
SeMoS	5.101	5.15-5.29

SeWS	4.738	4.22-4.75

Table 2. 1 Theoretically calculated and experimentally observed work function values for Janus material and their parent TMDc.

It can be seen from Fig 3.13 (a) that the work function of each domain varies in the range of 4.73 – 4.83 eV for the SeWS monolayer. The PL and Raman data were taken at room temperature from each visible domain with an objective of a 100x magnification. Here, in fig 3.13 (b) we have not observed a clear correlation between the work function of each domain and the PL peak position obtained at room temperature.

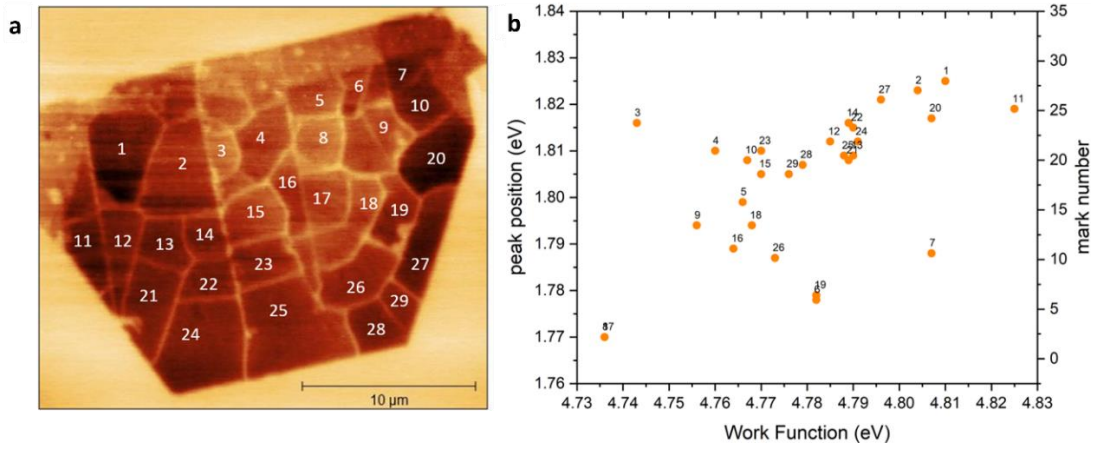

Fig 3. 13 a. Surface potential scan for SeWS sample 1, domains have been labeled for calculating work function for each of them b. PL peak position versus work function for SeWS monolayer.

The same analysis was performed for another sample to confirm the observed behavior Fig 3.14. It can be seen in Fig. 3.14 that the work function of individual grains varies within a much larger range compared to sample 1. This value range is from 4.22 to 4.78 eV. For this monolayer, there is also no correlation between work function and PL

peak position, which confirms the behavior observed for the first sample. We expect that at low-temperature, PL measurements of each grain would show defect-related emission for which its intensity or energy position could correlate with work function values. It was previously shown for CVD-grown WS_2 monolayer that defect density variation causes work function changes while the PL behavior also varies significantly across the monolayer. The mentioned difference in work function values due to changes in defect density can be as significant as 0.5 eV [113].

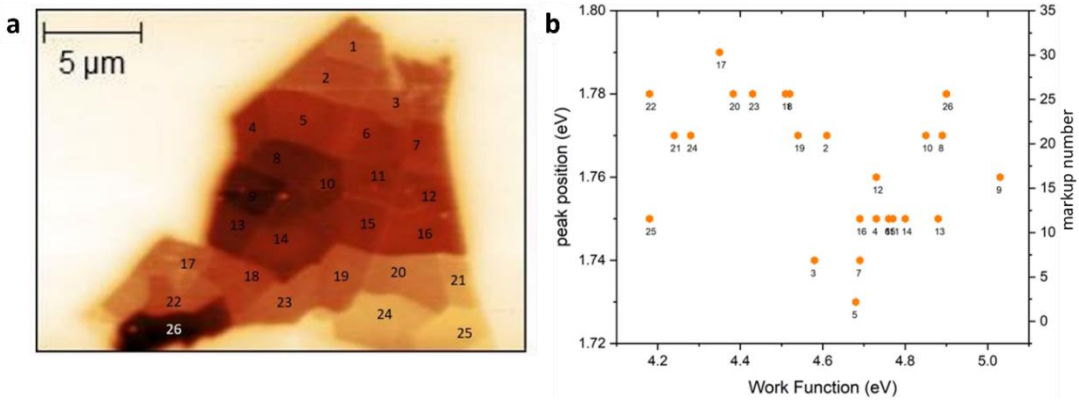

Fig 3. 14 a. Surface potential scan for SeWS sample 2. b. PL peak position Vs. work function graph for SeWS.

Chapter 4 – Identification and Analysis of surface phenomenon in Janus materials synthesized by pulsed laser deposition (PLD)

The success in utilizing the SEAR technique for synthesizing Janus crystal has opened up new research directions for studying the unique optical, electronic, and magnetic properties of this new material system. However, different synthesis routes can be explored for expanding the Janus materials library. This chapter discusses the results of AFM and KPFM studies for Janus monolayers synthesized by the pulsed laser deposition technique. We have described the emergence of different surface and electrical properties and compared them with results obtained for Janus materials synthesized by the SEAR process.

4.1. Synthesis of SWSe and SMoSe Janus monolayer by PLD process

For the synthesis of SMoSe and SWSe Janus crystal by PLD, instead of $MoSe_2$ or WSe_2, we used MoS_2 and WS_2 as the parent TMDc. There were two reasons behind this selection; first, we wanted to explore a different route for synthesizing SMoSe and SWSe, so the pulsed laser deposition technique was used for this experiment. Secondly, it was interesting to observe the morphological changes occurring because of the different sequences of the chalcogen layers in the as-synthesized Janus structure, namely Se on the top and S on the bottom. As the starting material was WS2 or MoS2, the Janus structure thus obtained had a Se layer on top and S on the bottom facet.

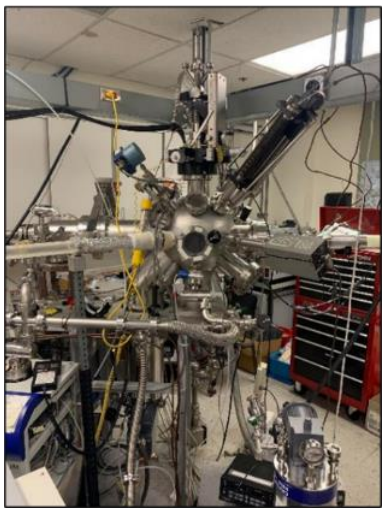

Fig 4. 1 Pulsed Laser Deposition (PLD) chamber.

For this experiment, the bulk crystal of WS_2 and MoS_2 were grown via CVT. In the case of WS_2, the synthesis procedure involved a two-step crystallization technique, similar to the one followed for $MoSe_2$. In the first step, elemental Tungsten (electronic grade purity 99.99%) and sublimation purified sulfur powder (99.9999% pure) were mixed in stoichiometric ratios and sealed in a quartz ampoule under vacuum of 10^{-6} torr. Afterward, the mixture was heated at 950ºCelsius for 5 days. For the second step, the pre-reacted powders were mixed with extra sulfur to reach a 1:2 stoichiometry along with trace amounts of $TeCl_4$ powder. Finally, all of the ingredients were resealed under 10^{-6} Torr, and the ampoule was kept in a high-temperature zone (1000ºC/950ºC) to activate the vapor transport mechanism for obtaining highly crystalline large single-crystal vdW WS_2 crystals after 65 hours of total growth time.

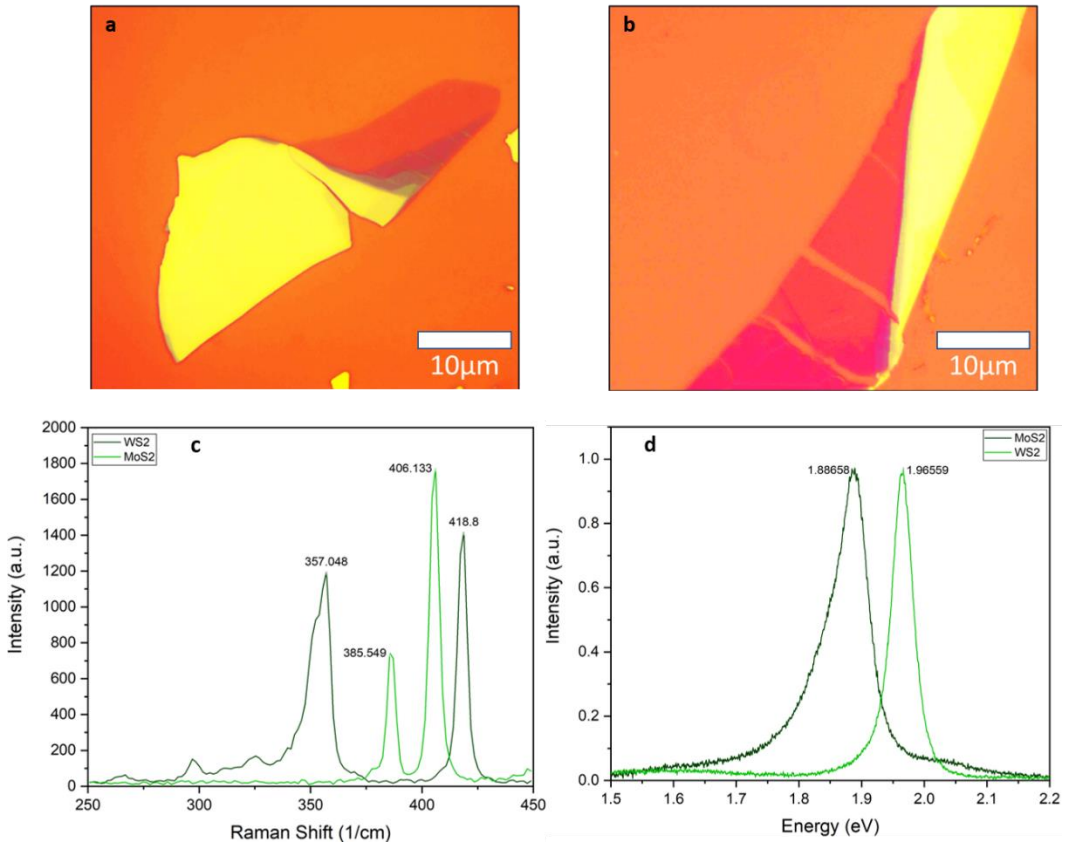

Fig 4. 2 a. WS_2 monolayer crystal on Si/SiO_2. b. MoS_2 crystal monolayer on Si/SiO_2. c. Raman spectra for MoS_2 and WS_2. d. Pl spectra for MoS_2 (FWHM = 55) and WS_2 (FWHM = 32) taken with 488 nm (blue) laser.

MoS_2 crystals used in these experiments were naturally occurring molybdenite crystals processed to procure thin crystals. The sample preparation for MoS_2 and WS_2 included exfoliation followed by checking PL and Raman spectra to confirm the thickness of the obtained samples. First, Si/SiO_2 substrates were ultrasonicated in ethanol, Acetone, and Isopropyl alcohol for 5 mins each, followed by blow-drying by UHP nitrogen. At last, substrates were O_2 plasma cleaned for 15 mins to eliminate residual organic contaminants. Next, bulk crystals for MoS_2 and WS_2 were put on scotch tape and

exfoliated until thin crystals were obtained on the tape. Afterward, a PDMS film was used to transfer the obtained thin crystals from tape to substrates. MoS_2 and WS_2 monolayers obtained by this method were identified under an optical microscope. By measuring PL emission, the thickness of these monolayers was confirmed.

The WS_2 and MoS_2 monolayer samples were pasted on a heating stage with silver paste and cured at 400ºC for 1 hour. The PLD chamber was kept at 10^{-8} torr and then flushed with 20 sccm UHP argon to bring the operating pressure to 10.5 mtorr. The reaction temperature of the chamber for SWSe conversion was set at 300ºC. The KrF excimer laser energy is set at 200 millijoules which hits a polished selenium target at an angle $\alpha \leq 45^{o}$ to generate a forward-directed plasma plume. This plasma plume consists of Se_2 and Se_9 clusters, of which Se_2 clusters with the highest energy at 3.52 eV are the dominant species interacting with the top layer chalcogen [98]. If the cluster energy is too high, it will knock the chalcogen and the metal atom, thus creating metal vacancies. With even higher energy, the cluster will start interacting with the bottom layer chalcogen and might lead to the generation of severe defects. The process is carried out for 6 mins and 45 seconds. Unlike SEAR, the conversion process occurs in one step. If the approaching Se_n cluster has just enough energy to knock the top chalcogen atoms and form a bond with the metal atom, then the process is less likely to cause defects [98]. If the cluster does not have the energy to break the bond between sulfur and underlying metal, then knocking and replacement will not happen. A very high-energy Se cluster might knock the top layer chalcogen, the metal atom, and sometimes the bottom layer chalcogen atom, too [98].

4.2. Investigation of wrinkling effect related to built-in-strain in SWSe and SMoSe monolayer

The topography analysis for PLD SWSe and SMoSe monolayers was performed by AFM. The AFM surface scans showed the morphological changes that happened due to the PLD process, as shown in Fig 4.3 (a, d). Synthesized Janus monolayers showed protuberances/wrinkling features ranging from 5 to 10 nm in height and 3 to 7 nm in width. A similar phenomenon was reported by Zheng *et al.*, where Janus monolayers of SMoSe and SWSe were synthesized by a low-energy implantation technique [114].

From the Raman spectra obtained for SWSe Fig. 4.3, (b), the A_1^1 mode position was determined to be at 284 cm^{-1} and for SMoSe at 286 cm^{-1}. Furthermore, the neutral exciton emission for SWSe was located at 1.81 eV and for SMoSe at 1.66 eV. These results are very similar to the results obtained for the Janus monolayer of SeWS and SeMoS synthesized by the SEAR process [74], [95]. However, the line width of the PL peak was slightly higher in the case of SMoSe (FWHM ~ 95 meV) and SWSe (FWHM ~ 80-85 meV) compared to the experimental results obtained for SEAR synthesized Janus monolayers. A larger value for line width may indicate a higher defect density induced by the PLD process.

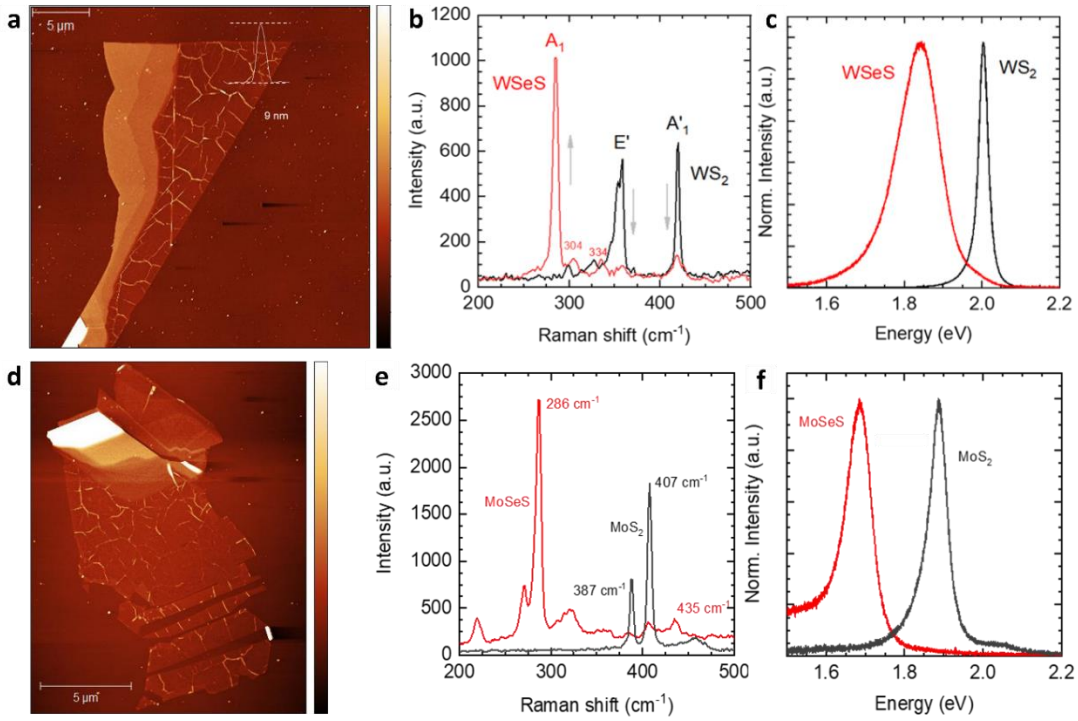

Fig 4. 3 a. AFM image of SWSe sample showing wrinkling features. Raman b. and PL c. spectra of SWSe and WS_2 parent TMDc. d. Wrinkling effect for the SMoSe. Raman e. and PL f. data for SMoSe and MoS_2.

The wrinkling effect seen in the AFM scans for Janus monolayers was thought to have originated from three possible mechanisms: (i) the difference in thermal expansion of monolayer and substrate due to the high temperature used for the process; (ii) the tensile strain created by the bombardment of Se atoms which might occupy interstitial positions; (iii) The creation of Janus structure where the top layer has build-up tensile strain due to replacement of S atoms by Se atoms and generation of defects, causing the formation of wrinkles.

For checking the first hypothesis, a WS_2 monolayer on SiO_2/Si substrate was prepared by mechanical exfoliation, mounted on a heating stage, and put inside the PLD chamber

(pressure inside chamber ~10^{-8} torr) at 400 °C for 1 hour. The sample was left to cool down to room temperature naturally inside the chamber at low pressure. Topography imaging of that sample was done before and after the annealing (Fig 4.4). The results obtained by AFM scans showed no wrinkles formed in the monolayer. Thus the hypothesis that the difference in the thermal expansion coefficient of monolayer and substrate is causing wrinkling was disproved.

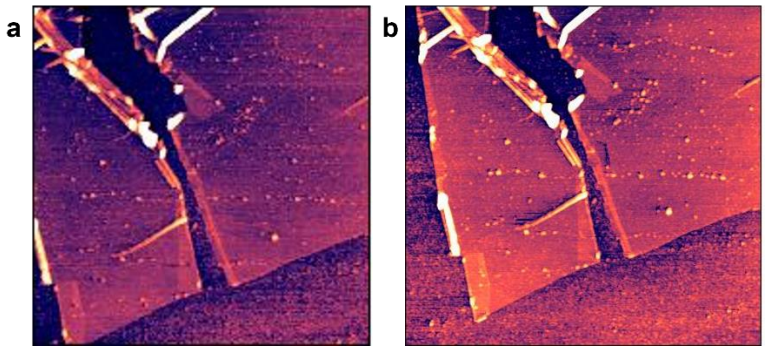

Fig 4. 4 AFM scans of WS_2 monolayer before a. and after b. annealing.

For testing the second hypothesis, a sample of WSe_2 was subjected to the same procedure as the one followed for synthesizing SWSe from WS_2 monolayers. The topography scan of the WSe_2 monolayer subjected to selenium bombardment revealed that no wrinkling features appeared on the monolayer as were found for SWSe or SMoSe. This confirmed that the aforementioned surface phenomena did not originate due to the strain caused by the Se bombardment.

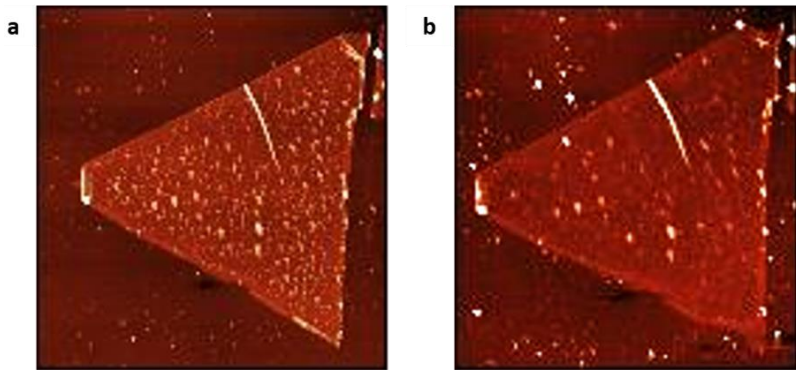

Fig 4. 5 AFM scan of monolayer WSe_2 before a. after b Selenium bombardment.

Disproving the first two hypotheses as the cause of wrinkle formation meant that the observed phenomena were due to the intrinsic properties of the Janus monolayer. Since SWSe and SMoSe Janus monolayers have selenium on the upper facet and sulfur on the bottom, they will experience built-in strain due to the significant difference in atomic radii of selenium and sulfur atoms. The asymmetry related to mentioned atomic radii differences causes the selenium layer to experience tensile strain and the sulfur layer a compressive strain. The monolayer cannot sustain that strain and start wrinkling, where sulfur atoms are pushed directly toward each other. Since the lateral forces are acting from opposing directions, the strained point of the monolayer keeps rising and forms protuberance in the form of wrinkle. The wrinkle will stop increasing in height due to the buildup of tensile strain in the remaining flat part of the monolayer. Hence, the formation of wrinkling features is related to the straining and the relaxation mechanism that happens throughout the monolayer during the process of Janus synthesis.

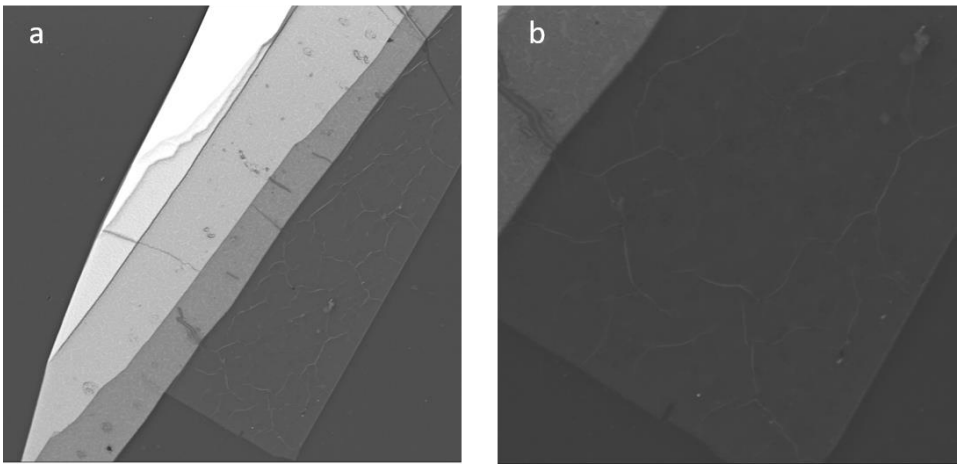

Fig 4. 6 a. SEM image of SeWS monolayer. b. close-up image of wrinkles.

From the close-up SEM image shown in Fig 4.6 (b), no features other than wrinkling can be seen on the monolayer. Moreover, the Janus monolayer is not divided into multiple domains due to cracking phenomena.

4.3. Studies of work function for SWSe and SMoSe monolayers by Kelvin probe force microscopy

The AFM scans obtained for SWSe, and SMoSe shows wrinkle formation but not cracking features as in the case of SEAR converted monolayers. Since wrinkles are formed across the whole monolayers, the objective was to check whether the mosaic pattern in surface potential would also appear for PLD converted sample. For that purpose, the SWSe, and SMoSe monolayers were measured by KPFM. Moreover, since the SEAR and PLD synthesized Janus monolayers are structurally the same material, we expect their work function to be the same. Therefore, this experiment also checked if

there were any differences in the work function of (SWSe / SMoSe) and (SeWS / SeMoS) Janus monolayers which would show the significance of substrate interaction.

As mentioned Kelvin probe force microscopy technique was used to determine the surface potential of the Janus monolayers, based on which the work function was also calculated. The scans were obtained at the NT-MDT Modular AFM instrument in second (II) pass AM-SKM tapping mode. The FMV-PT probe with Pt-Ir coating was used for this electrical measurement. Janus monolayers were raster-scanned in a horizontal orientation with 512-pixel/lines at 0.2 Hz. Biasing voltage of 1 V AC was applied to the substrate, and the DC feedback value was modulated to nullify the contact potential difference for each sample accordingly.

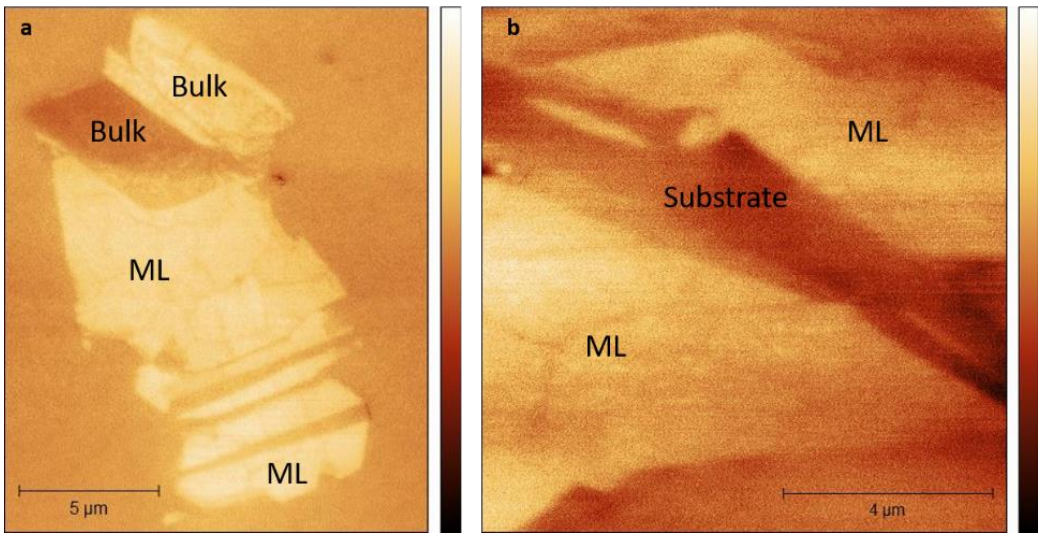

Fig 4. 7 Surface potential plot for a. SMoSe and b. SWSe monolayers.

From Fig 4.7, it was calculated that Janus monolayers of SWSe showed a variation of work function in the range of 4.69 – 4.73 eV. While for the SMoSe monolayer, the work

function value changes between 5.01 – 5.07 eV. Furthermore, no mosaic pattern formation was observed, as was seen for SEAR synthesized Janus monolayers. The only observed changes across monolayer are related to areas where wrinkles are formed. It can be seen that in these areas, surface potential/work function is lower/higher. Moreover, for the remaining part of the monolayer work function is uniform. The work function for SWSe and SMoSe monolayers was calculated from the equation; $Ø_{Sample} = Ø_{Tip} - V_{CPD}$, where on the right-hand side of the equation is respectively the work function of a tip and measured surface potential difference. The table below summarizes the work function values calculated (by the same approach which was mentioned in chapter 3.3.1) for WS_2, MoS_2, SWSe, and SMoSe monolayer samples. The PLD synthesized Janus materials show different values for work function compared to the experimentally observed value for SEAR synthesized samples. The reason for this difference can be related to the various defect densities or the reversed orientation of the built-in e-field in the Janus monolayers, which matter for monolayer substrate interaction.

Material	**Theoretical value of Ø sample (eV)**	**Experimentally observed value of Ø sample (eV)**
MoS_2	5.053	5.017
WS_2	4.697	4.672
SMoSe	5.101	5.01-5.07
SWSe	4.738	4.69-4.73

Table 3. 1 Theoretically calculated vs. experimentally observed values for Janus material and their parent TMDc.

Conclusions and Future Directions

This work has introduced the microscale defects and imperfections in 2D Janus materials for the first time in the literature. Comprehensive studies were carried out to convert 2D classical Mo and W-based direct semiconductors into 2D Janus semiconductors using two distinct techniques, namely SEAR (selective epitaxy atomic replacement) and PLD (pulsed laser deposition). Using Raman, PL, SEM/EDS, and microscopy techniques, the studies have shown that microscale defects, namely fractures and cracking, form in 2D Janus layers. Interestingly, those 2D Janus materials produced through the SEAR process exhibit physical cracking features while 2D Janus layers from PLD samples show wrinkling behavior. Our studies indicate that these features are ultimately related to surface compressive and tensile stress built-in 2D Janus layers depending on their atomic surface order. More specifically, SEAR SeMS (M=Mo, W) samples exhibit tensile strain at the substrate / 2D Janus interface (as the selenium is facing the surface and Se has a much larger Bohr radius compared to S), and this internal strain causes physical cracking. In contrast, PLD-grown SMSe (M=Mo and W) 2D Janus layers cannot contain the compressive strain at the 2D Janus/substrate interface (as the sulfur is facing the surface and has a much smaller Bohr radius compared to Se), and this causes wrinkling (out of plane bulging) behavior in these 2D thin films.

Additional optical, vibrational, and structural characterization was performed to correlate how the imperfections influence their overall physical properties to establish process-structure-property relations. Overall results have shown that these microscale

imperfects primarily influence the surface potential variations [115], edge state charge cumulation [116], and other vibrational (phononic) properties [117]. The results herein introduced these imperfections in 2D Janus layers and assigned their physical signatures to the electronic properties of these newly emergent material systems. Overall conclusions can be summarized in the bulled form below

1. For Janus monolayer SeMS (M = W/Mo) synthesized through the SEAR technique, surface cracking is observed for sulfur atoms as the top facet of the surface.
2. Janus monolayers SMSe (M = W/Mo) produced via pulsed laser deposition were shown to develop wrinkling features on the surface, where selenium decorated the top facet of the crystal.
3. These microscale features (cracking and wrinkling) influence surface potential characteristics across the Janus monolayers.

Janus monolayer synthesized via PLD might be more suitable for electronic devices since the 2D layers are still continuous without any physical discontinuity, unlike the monolayers produced with the SEAR technique.

5.1. Future studies

Considering the advances made by these studies, we foresee that the following directions must be explored in greater detail. Firstly, new manufacturing processes must be discovered, or the existing ones must be modified to create 2D Janus layers without microscale defects such as cracking or wrinkling. While it is nearly impossible to comment on the new manufacturing directions, mild plasma processing techniques or

temperature variable SEAR or PLD processes might be useful to prevent these microscale defects.

Another potential direction is to better understand the excitonic, magnetic, vibrational, and electronic properties of these cracks (edge states) or wrinkled regions (nanoscale strains). Previous studies on classical 2D layers (MoS_2 [118], graphene [119] etc.) have already shown that the presence of edge states or strained regions lead to new effects including edge state PL emission [119], [120], edge magnetism [121], solar funnel effect in nanoscale strained regions [122]. While these studies have introduced these defects artificially, 2D Janus layers naturally host these defects [123]. More studies will be needed to shed a light on how the presence of these microscale defects change their excitonic, magnetic, thermal, and electronic properties. More specifically, many crucial fundamental questions will need to be addressed to better understand their macroscale properties of these 2D Janus films. Examples to these fundamental questions include but not limited to;

1. How does the excitonic emission wavelength as well as efficiency are influenced by microscale defects?
2. Is there a band-renormalizations and band gap variation in strain engineered (buckled) regions?
3. What is the macroscale electronic properties of these 2D Janus layers in the presence of these microscale defects?
4. Do these edge states around cracking host edge luminescence, edge magnetism, or edge conductivity?

Last area of future study is likely to involve the atomic scale imperfections. While this thesis addresses, microscale defects in 2D Janus layers, additional studies must take this domain to atomic scales to introduce how SEAR or PLD processes introduce point defects (vacancy, substitutional, etc.). STEM or TEM measurements will be absolutely required to establish the atomic defect library of 2D Janus layers to better correlate process-structure-property relations of these new material systems for their meaningful transition to electronic, information science, and quantum information applications.

REFERENCES

[1] A. K. Almuhammady, K. F. M. Salem, M. T. Alloosh, M. M. Saleh, L. M. Alnaddaf, and J. M. Al-Khayri, "Nanomaterials Fundamentals: Classification, Synthesis and Characterization," in *Nanobiotechnology : Mitigation of Abiotic Stress in Plants*, J. M. Al-Khayri, M. I. Ansari, and A. K. Singh, Eds. Cham: Springer International Publishing, 2021, pp. 77–99. doi: 10.1007/978-3-030-73606-4_4.

[2] K. S. Novoselov *et al.*, "Electric field effect in atomically thin carbon films," *Science*, vol. 306, no. 5696, pp. 666–669, Oct. 2004, doi: 10.1126/science.1102896.

[3] A. H. Castro Neto, F. Guinea, N. M. R. Peres, K. S. Novoselov, and A. K. Geim, "The electronic properties of graphene," *Rev. Mod. Phys.*, vol. 81, no. 1, pp. 109–162, Jan. 2009, doi: 10.1103/RevModPhys.81.109.

[4] S.-W. Ng, N. Noor, and Z. Zheng, "Graphene-based two-dimensional Janus materials," *NPG Asia Mater*, vol. 10, no. 4, Art. no. 4, Apr. 2018, doi: 10.1038/s41427-018-0023-8.

[5] K. I. Bolotin *et al.*, "Ultrahigh electron mobility in suspended graphene," *Solid State Communications*, vol. 146, no. 9–10, pp. 351–355, Jun. 2008, doi: 10.1016/j.ssc.2008.02.024.

[6] A. A. Balandin *et al.*, "Superior Thermal Conductivity of Single-Layer Graphene," *Nano Lett.*, vol. 8, no. 3, pp. 902–907, Mar. 2008, doi: 10.1021/nl0731872.

[7] I. W. Frank, D. M. Tanenbaum, A. M. van der Zande, and P. L. McEuen, "Mechanical properties of suspended graphene sheets," *Journal of Vacuum Science & Technology B: Microelectronics and Nanometer Structures Processing, Measurement, and Phenomena*, vol. 25, no. 6, pp. 2558–2561, Nov. 2007, doi: 10.1116/1.2789446.

[8] A. K. Geim and K. S. Novoselov, "The rise of graphene," in *Nanoscience and Technology*, Co-Published with Macmillan Publishers Ltd, UK, 2009, pp. 11–19. doi: 10.1142/9789814287005_0002.

[9] K. S. Novoselov *et al.*, "Two-dimensional gas of massless Dirac fermions in graphene," *Nature*, vol. 438, no. 7065, pp. 197–200, Nov. 2005, doi: 10.1038/nature04233.

[10] Y. Zhang, Y.-W. Tan, H. L. Stormer, and P. Kim, "Experimental observation of the quantum Hall effect and Berry's phase in graphene," *Nature*, vol. 438, no. 7065, Art. no. 7065, Nov. 2005, doi: 10.1038/nature04235.

[11] Z. Zhou *et al.*, “Enhancing stability by tuning element ratio in 2D transition metal chalcogenides,” *Nano Res.*, vol. 14, no. 6, pp. 1704–1710, Jun. 2021, doi: 10.1007/s12274-020-3035-y.

[12] K. F. Mak, C. Lee, J. Hone, J. Shan, and T. F. Heinz, “Atomically Thin MoS 2 : A New Direct-Gap Semiconductor,” *Phys. Rev. Lett.*, vol. 105, no. 13, p. 136805, Sep. 2010, doi: 10.1103/PhysRevLett.105.136805.

[13] A. Splendiani *et al.*, “Emerging Photoluminescence in Monolayer MoS2,” *Nano Lett.*, vol. 10, no. 4, pp. 1271–1275, Apr. 2010, doi: 10.1021/nl903868w.

[14] Q. H. Wang, K. Kalantar-Zadeh, A. Kis, J. N. Coleman, and M. S. Strano, “Electronics and optoelectronics of two-dimensional transition metal dichalcogenides,” *Nature Nanotech*, vol. 7, no. 11, Art. no. 11, Nov. 2012, doi: 10.1038/nnano.2012.193.

[15] J. Kang, S. Tongay, J. Li, and J. Wu, “Monolayer semiconducting transition metal dichalcogenide alloys: Stability and band bowing,” *Journal of Applied Physics*, vol. 113, no. 14, p. 143703, Apr. 2013, doi: 10.1063/1.4799126.

[16] H. Terrones *et al.*, “New First Order Raman-active Modes in Few Layered Transition Metal Dichalcogenides,” *Sci Rep*, vol. 4, no. 1, Art. no. 1, Feb. 2014, doi: 10.1038/srep04215.

[17] K. Parvez, “Chapter 1 - Two-Dimensional Nanomaterials: Crystal Structure and Synthesis,” in *Biomedical Applications of Graphene and 2D Nanomaterials*, M. Nurunnabi and J. R. McCarthy, Eds. Elsevier, 2019, pp. 1–25. doi: 10.1016/B978-0-12-815889-0.00001-5.

[18] A. Kuc, “Low-dimensional transition-metal dichalcogenides,” pp. 1–29, 2014, doi: 10.1039/9781782620112-00001.

[19] J. Ribeiro-Soares *et al.*, “Group theory analysis of phonons in two-dimensional transition metal dichalcogenides,” *Phys. Rev. B*, vol. 90, no. 11, p. 115438, Sep. 2014, doi: 10.1103/PhysRevB.90.115438.

[20] R. Saito, Y. Tatsumi, S. Huang, X. Ling, and M. S. Dresselhaus, “Raman spectroscopy of transition metal dichalcogenides,” *J. Phys.: Condens. Matter*, vol. 28, no. 35, p. 353002, Jul. 2016, doi: 10.1088/0953-8984/28/35/353002.

[21] G. Wang *et al.*, “Colloquium: Excitons in atomically thin transition metal dichalcogenides,” *Rev. Mod. Phys.*, vol. 90, no. 2, p. 021001, Apr. 2018, doi: 10.1103/RevModPhys.90.021001.

[22] D. Jariwala, V. K. Sangwan, L. J. Lauhon, T. J. Marks, and M. C. Hersam, “Emerging Device Applications for Semiconducting Two-Dimensional Transition

Metal Dichalcogenides," *ACS Nano*, vol. 8, no. 2, pp. 1102–1120, Feb. 2014, doi: 10.1021/nn500064s.

[23] D. W. Latzke *et al.*, "Electronic structure, spin-orbit coupling, and interlayer interaction in bulk ${\mathrm{MoS}}_{2}$ and ${\mathrm{WS}}_{2}$," *Phys. Rev. B*, vol. 91, no. 23, p. 235202, Jun. 2015, doi: 10.1103/PhysRevB.91.235202.

[24] M. Chhowalla, Z. Liu, and H. Zhang, "Two-dimensional transition metal dichalcogenide (TMD) nanosheets," *Chem. Soc. Rev.*, vol. 44, no. 9, pp. 2584–2586, Apr. 2015, doi: 10.1039/C5CS90037A.

[25] S. Wu *et al.*, "Electrical tuning of valley magnetic moment through symmetry control in bilayer MoS2," *Nature Phys*, vol. 9, no. 3, Art. no. 3, Mar. 2013, doi: 10.1038/nphys2524.

[26] K. F. Mak, K. He, J. Shan, and T. F. Heinz, "Control of valley polarization in monolayer MoS2 by optical helicity," *Nat Nanotechnol*, vol. 7, no. 8, pp. 494–498, Aug. 2012, doi: 10.1038/nnano.2012.96.

[27] "Valley polarization in MoS2 monolayers by optical pumping | Nature Nanotechnology." https://www.nature.com/articles/nnano.2012.95 (accessed May 22, 2022).

[28] K.-A. N. Duerloo, M. T. Ong, and E. J. Reed, "Intrinsic Piezoelectricity in Two-Dimensional Materials," *J. Phys. Chem. Lett.*, vol. 3, no. 19, pp. 2871–2876, Oct. 2012, doi: 10.1021/jz3012436.

[29] R. H. Friend and A. D. Yoffe, "Electronic properties of intercalation complexes of the transition metal dichalcogenides," *Advances in Physics*, vol. 36, no. 1, pp. 1–94, Jan. 1987, doi: 10.1080/00018738700101951.

[30] S. Manzeli, D. Ovchinnikov, D. Pasquier, O. V. Yazyev, and A. Kis, "2D transition metal dichalcogenides," *Nat Rev Mater*, vol. 2, no. 8, Art. no. 8, Jun. 2017, doi: 10.1038/natrevmats.2017.33.

[31] Y. Wang *et al.*, "Strain-induced direct–indirect bandgap transition and phonon modulation in monolayer WS2," *Nano Res.*, vol. 8, no. 8, pp. 2562–2572, Aug. 2015, doi: 10.1007/s12274-015-0762-6.

[32] H. R. Gutiérrez *et al.*, "Extraordinary Room-Temperature Photoluminescence in Triangular WS2 Monolayers," *Nano Lett.*, vol. 13, no. 8, pp. 3447–3454, Aug. 2013, doi: 10.1021/nl3026357.

[33] M. Zulfiqar, Y. Zhao, G. Li, Z. Li, and J. Ni, "Intrinsic Thermal conductivities of monolayer transition metal dichalcogenides MX2 (M = Mo, W; X = S, Se, Te)," *Sci Rep*, vol. 9, no. 1, Art. no. 1, Mar. 2019, doi: 10.1038/s41598-019-40882-2.

[34] A. Kumar and P. K. Ahluwalia, “Electronic structure of transition metal dichalcogenides monolayers 1H-MX2 (M = Mo, W; X = S, Se, Te) from ab-initio theory: new direct band gap semiconductors,” *Eur. Phys. J. B*, vol. 85, no. 6, p. 186, Jun. 2012, doi: 10.1140/epjb/e2012-30070-x.

[35] S.-J. Lee *et al.*, “Programmable devices based on reversible solid-state doping of two-dimensional semiconductors with superionic silver iodide,” *Nat Electron*, vol. 3, no. 10, Art. no. 10, Oct. 2020, doi: 10.1038/s41928-020-00472-x.

[36] J.-W. Chen *et al.*, “A gate-free monolayer WSe2 pn diode,” *Nat Commun*, vol. 9, no. 1, Art. no. 1, Aug. 2018, doi: 10.1038/s41467-018-05326-x.

[37] C. J. Gil, A. Pham, A. Yu, and S. Li, “An ab initio study of transition metals doped with WSe2 for long-range room temperature ferromagnetism in two-dimensional transition metal dichalcogenide,” *J Phys Condens Matter*, vol. 26, no. 30, p. 306004, Jul. 2014, doi: 10.1088/0953-8984/26/30/306004.

[38] B. Lei *et al.*, “Significantly enhanced optoelectronic performance of tungsten diselenide phototransistor via surface functionalization,” *Nano Res.*, vol. 10, no. 4, pp. 1282–1291, Apr. 2017, doi: 10.1007/s12274-016-1386-1.

[39] P. Joensen, R. F. Frindt, and S. R. Morrison, “Single-layer MoS2,” *Materials Research Bulletin*, vol. 21, no. 4, pp. 457–461, Apr. 1986, doi: 10.1016/0025-5408(86)90011-5.

[40] R. F. Frindt *et al.*, “Exfoliated MoS_2 monolayers as substrates for magnetic materials,” *Journal of Applied Physics*, vol. 70, no. 10, pp. 6224–6226, Nov. 1991, doi: 10.1063/1.350002.

[41] Y. Iwakabe, M. Hara, K. Kondo, S. Oh-Hara, and A. M. Sasabe, “Anchoring Structure of Binary Mixture of Liquid Crystals Studied by Scanning Tunneling Microscopy,” *Jpn. J. Appl. Phys.*, vol. 31, no. 12B, p. L1771, Dec. 1992, doi: 10.1143/JJAP.31.L1771.

[42] A. Manivannan *et al.*, “Scanning Probe Microscopic Investigation of Epitaxially Grown C60 Film on MoS2,” *Jpn. J. Appl. Phys.*, vol. 31, no. 11R, p. 3680, Nov. 1992, doi: 10.1143/JJAP.31.3680.

[43] J. Park, N. Choudhary, J. Smith, G. Lee, M. Kim, and W. Choi, “Thickness modulated MoS2 grown by chemical vapor deposition for transparent and flexible electronic devices,” *Appl. Phys. Lett.*, vol. 106, no. 1, p. 012104, Jan. 2015, doi: 10.1063/1.4905476.

[44] L. Jiang *et al.*, “Monolayer MoS2–Graphene Hybrid Aerogels with Controllable Porosity for Lithium-Ion Batteries with High Reversible Capacity,” *ACS Appl. Mater. Interfaces*, vol. 8, no. 4, pp. 2680–2687, Feb. 2016, doi: 10.1021/acsami.5b10692.

[45] S. Ghatak, A. N. Pal, and A. Ghosh, “Nature of Electronic States in Atomically Thin MoS2 Field-Effect Transistors,” *ACS Nano*, vol. 5, no. 10, pp. 7707–7712, Oct. 2011, doi: 10.1021/nn202852j.

[46] D. J. Late, B. Liu, H. S. S. R. Matte, V. P. Dravid, and C. N. R. Rao, “Hysteresis in Single-Layer MoS2 Field Effect Transistors,” *ACS Nano*, vol. 6, no. 6, pp. 5635–5641, Jun. 2012, doi: 10.1021/nn301572c.

[47] H. Li, J. Wu, Z. Yin, and H. Zhang, “Preparation and Applications of Mechanically Exfoliated Single-Layer and Multilayer MoS2 and WSe2 Nanosheets,” *Acc. Chem. Res.*, vol. 47, no. 4, pp. 1067–1075, Apr. 2014, doi: 10.1021/ar4002312.

[48] O. Samy, S. Zeng, M. D. Birowosuto, and A. El Moutaouakil, “A Review on MoS2 Properties, Synthesis, Sensing Applications and Challenges,” *Crystals*, vol. 11, no. 4, Art. no. 4, Apr. 2021, doi: 10.3390/cryst11040355.

[49] M. Kan *et al.*, “Structures and Phase Transition of a MoS2 Monolayer,” *J. Phys. Chem. C*, vol. 118, no. 3, pp. 1515–1522, Jan. 2014, doi: 10.1021/jp4076355.

[50] A. Jawaid *et al.*, “Mechanism for Liquid Phase Exfoliation of MoS2,” *Chem. Mater.*, vol. 28, no. 1, pp. 337–348, Jan. 2016, doi: 10.1021/acs.chemmater.5b04224.

[51] Q. Tang and D. Jiang, “Stabilization and Band-Gap Tuning of the 1T-MoS2 Monolayer by Covalent Functionalization,” *Chem. Mater.*, vol. 27, no. 10, pp. 3743–3748, May 2015, doi: 10.1021/acs.chemmater.5b00986.

[52] X. Huang, Z. Zeng, and H. Zhang, “Metal dichalcogenide nanosheets : preparation, properties and applications,” *Chemical Society Reviews*, vol. 42, no. 5, pp. 1934–1946, 2013, doi: 10.1039/C2CS35387C.

[53] R. Sha, P. C. Maity, U. Rajaji, T.-Y. Liu, and T. K. Bhattacharyya, “Review—MoSe$\less$sub$\greater$2$\less$/sub$\greater$ Nanostructures and Related Electrodes for Advanced Supercapacitor Developments,” *J. Electrochem. Soc.*, vol. 169, no. 1, p. 013503, Jan. 2022, doi: 10.1149/1945-7111/ac4aad.

[54] X. Zhou *et al.*, “Tubular Photodetectors: Rolling up MoSe2 Nanomembranes as a Sensitive Tubular Photodetector (Small 42/2019),” *Small*, vol. 15, no. 42, p. 1970229, 2019, doi: 10.1002/smll.201970229.

[55] X. Wu, Y. Wang, P. Li, and Z. Xiong, “Research status of MoSe2 and its composites: A review,” *Superlattices and Microstructures*, vol. 139, p. 106388, Mar. 2020, doi: 10.1016/j.spmi.2020.106388.

[56] H. Tang, K. Dou, C.-C. Kaun, Q. Kuang, and S. Yang, “MoSe2 nanosheets and their graphene hybrids: synthesis, characterization and hydrogen evolution reaction

studies," *J. Mater. Chem. A*, vol. 2, no. 2, pp. 360–364, Dec. 2013, doi: 10.1039/C3TA13584E.

[57] P. Tonndorf *et al.*, "Photoluminescence emission and Raman response of monolayer MoS_2, $MoSe_2$, and WSe_2," *Opt. Express, OE*, vol. 21, no. 4, pp. 4908–4916, Feb. 2013, doi: 10.1364/OE.21.004908.

[58] T. Chen *et al.*, "Controlled growth of atomically thin MoSe $\less$sub$\greater$2$\less$/sub$\greater$ films and nanoribbons by chemical vapor deposition," *2D Mater.*, vol. 6, no. 2, p. 025002, Jan. 2019, doi: 10.1088/2053-1583/aaf9cc.

[59] A. Ohtake and Y. Sakuma, "Heteroepitaxy of MoSe2 on Si(111) substrates: Role of surface passivation," *Appl. Phys. Lett.*, vol. 114, no. 5, p. 053106, Feb. 2019, doi: 10.1063/1.5083974.

[60] Z. Zeng *et al.*, "Single-Layer Semiconducting Nanosheets: High-Yield Preparation and Device Fabrication," *Angewandte Chemie*, vol. 123, no. 47, pp. 11289–11293, 2011, doi: 10.1002/ange.201106004.

[61] S. Yang *et al.*, "Tuning the Optical, Magnetic, and Electrical Properties of ReSe2 by Nanoscale Strain Engineering," *Nano Lett.*, vol. 15, no. 3, pp. 1660–1666, Mar. 2015, doi: 10.1021/nl504276u.

[62] X. Zhang and Q. Li, "Electronic and magnetic properties of nonmetal atoms adsorbed ReS2 monolayers," *Journal of Applied Physics*, vol. 118, no. 6, p. 064306, Aug. 2015, doi: 10.1063/1.4928460.

[63] S. Tongay *et al.*, "Monolayer behaviour in bulk ReS2 due to electronic and vibrational decoupling," *Nat Commun*, vol. 5, no. 1, Art. no. 1, Feb. 2014, doi: 10.1038/ncomms4252.

[64] M. Rahman, K. Davey, and S.-Z. Qiao, "Advent of 2D Rhenium Disulfide (ReS2): Fundamentals to Applications," *Advanced Functional Materials*, vol. 27, no. 10, p. 1606129, 2017, doi: 10.1002/adfm.201606129.

[65] K. Friemelt *et al.*, "Optical and photoelectrical properties of ReS2 single crystals," *Journal of Applied Physics*, vol. 79, no. 12, pp. 9268–9272, Jun. 1996, doi: 10.1063/1.362602.

[66] R. He *et al.*, "Coupling and Stacking Order of ReS2 Atomic Layers Revealed by Ultralow-Frequency Raman Spectroscopy," *Nano Lett.*, vol. 16, no. 2, pp. 1404–1409, Feb. 2016, doi: 10.1021/acs.nanolett.5b04925.

[67] H. Wang *et al.*, "High-quality monolayer superconductor NbSe2 grown by chemical vapour deposition," *Nat Commun*, vol. 8, no. 1, Art. no. 1, Aug. 2017, doi: 10.1038/s41467-017-00427-5.

[68] Z. Xu *et al.*, “Topical review: recent progress of charge density waves in 2D transition metal dichalcogenide-based heterojunctions and their applications,” *Nanotechnology*, vol. 32, no. 49, p. 492001, Sep. 2021, doi: 10.1088/1361-6528/ac21ed.

[69] X. Xi *et al.*, “Strongly enhanced charge-density-wave order in monolayer NbSe2,” *Nature Nanotech*, vol. 10, no. 9, Art. no. 9, Sep. 2015, doi: 10.1038/nnano.2015.143.

[70] C. Ruppert, O. B. Aslan, and T. F. Heinz, “Optical Properties and Band Gap of Single- and Few-Layer MoTe2 Crystals,” *Nano Lett.*, vol. 14, no. 11, pp. 6231–6236, Nov. 2014, doi: 10.1021/nl502557g.

[71] X. Sun, P. Bonnick, and L. F. Nazar, “Layered TiS2 Positive Electrode for Mg Batteries,” *ACS Energy Lett.*, vol. 1, no. 1, pp. 297–301, Jul. 2016, doi: 10.1021/acsenergylett.6b00145.

[72] D. Wolverson, S. Crampin, A. S. Kazemi, A. Ilie, and S. J. Bending, “Raman Spectra of Monolayer, Few-Layer, and Bulk ReSe2: An Anisotropic Layered Semiconductor,” *ACS Nano*, vol. 8, no. 11, pp. 11154–11164, Nov. 2014, doi: 10.1021/nn5053926.

[73] L. Ju, M. Bie, J. Shang, X. Tang, and L. Kou, “Janus transition metal dichalcogenides: a superior platform for photocatalytic water splitting,” *J. Phys. Mater.*, vol. 3, no. 2, p. 022004, Apr. 2020, doi: 10.1088/2515-7639/ab7c57.

[74] D. B. Trivedi *et al.*, “Room-Temperature Synthesis of 2D Janus Crystals and their Heterostructures,” *Advanced Materials*, vol. 32, no. 50, p. 2006320, 2020, doi: 10.1002/adma.202006320.

[75] C. Zhang, Y. Nie, S. Sanvito, and A. Du, “First-Principles Prediction of a Room-Temperature Ferromagnetic Janus VSSe Monolayer with Piezoelectricity, Ferroelasticity, and Large Valley Polarization,” *Nano Lett.*, vol. 19, no. 2, pp. 1366–1370, Feb. 2019, doi: 10.1021/acs.nanolett.8b05050.

[76] L. Hu and D. Wei, “Janus Group-III Chalcogenide Monolayers and Derivative Type-II Heterojunctions as Water-Splitting Photocatalysts with Strong Visible-Light Absorbance,” *J. Phys. Chem. C*, vol. 122, no. 49, pp. 27795–27802, Dec. 2018, doi: 10.1021/acs.jpcc.8b06575.

[77] R. Chaurasiya and A. Dixit, “Defect engineered MoSSe Janus monolayer as a promising two dimensional material for NO2 and NO gas sensing,” *Applied Surface Science*, vol. 490, pp. 204–219, Oct. 2019, doi: 10.1016/j.apsusc.2019.06.049.

[78] Y. Cheng, Z. Zhu, M. Tahir, and U. Schwingenschlögl, “Spin-orbit-induced spin splittings in polar transition metal dichalcogenide monolayers,” Jun. 2013,

Accessed: May 24, 2022. [Online]. Available: https://repository.kaust.edu.sa/handle/10754/562800

[79] Yu. A. Bychkov, V. I. Mel'nikov, and E. I. Rashba, "Effect of spin-orbit coupling on the energy spectrum of a 2D electron system in a tilted magnetic field," *Soviet Journal of Experimental and Theoretical Physics*, vol. 71, p. 401, Aug. 1990.

[80] Q.-F. Yao *et al.*, "Manipulation of the large Rashba spin splitting in polar two-dimensional transition-metal dichalcogenides," *Phys. Rev. B*, vol. 95, no. 16, p. 165401, Apr. 2017, doi: 10.1103/PhysRevB.95.165401.

[81] W. Zhou, J. Chen, Z. Yang, J. Liu, and F. Ouyang, "Geometry and electronic structure of monolayer, bilayer, and multilayer Janus WSSe," *Phys. Rev. B*, vol. 99, no. 7, p. 075160, Feb. 2019, doi: 10.1103/PhysRevB.99.075160.

[82] Y. Chen, Q. Fan, Y. Liu, and G. Yao, "Electrically tunable magnetism and unique intralayer charge transfer in Janus monolayer MnSSe for spintronics applications," *Phys. Rev. B*, vol. 105, no. 19, p. 195410, May 2022, doi: 10.1103/PhysRevB.105.195410.

[83] M. Yagmurcukardes *et al.*, "Quantum properties and applications of 2D Janus crystals and their superlattices," *Applied Physics Reviews*, vol. 7, no. 1, p. 011311, Mar. 2020, doi: 10.1063/1.5135306.

[84] J. Liang *et al.*, "Very large Dzyaloshinskii-Moriya interaction in two-dimensional Janus manganese dichalcogenides and its application to realize skyrmion states," *Phys. Rev. B*, vol. 101, no. 18, p. 184401, May 2020, doi: 10.1103/PhysRevB.101.184401.

[85] F. Li, W. Wei, H. Wang, B. Huang, Y. Dai, and T. Jacob, "Intrinsic Electric Field-Induced Properties in Janus MoSSe van der Waals Structures," *J. Phys. Chem. Lett.*, vol. 10, no. 3, pp. 559–565, Feb. 2019, doi: 10.1021/acs.jpclett.8b03463.

[86] A. C. Riis-Jensen, M. Pandey, and K. S. Thygesen, "Efficient Charge Separation in 2D Janus van der Waals Structures with Built-in Electric Fields and Intrinsic p–n Doping," *J. Phys. Chem. C*, vol. 122, no. 43, pp. 24520–24526, Nov. 2018, doi: 10.1021/acs.jpcc.8b05792.

[87] M. A. U. Absor, H. Kotaka, F. Ishii, and M. Saito, "Tunable spin splitting and spin lifetime in polar WSTe monolayer," *Jpn. J. Appl. Phys.*, vol. 57, no. 4S, p. 04FP01, Feb. 2018, doi: 10.7567/JJAP.57.04FP01.

[88] J. Zhang *et al.*, "Janus Monolayer Transition-Metal Dichalcogenides," *ACS Nano*, vol. 11, no. 8, pp. 8192–8198, Aug. 2017, doi: 10.1021/acsnano.7b03186.

[89] A.-Y. Lu *et al.*, "Janus monolayers of transition metal dichalcogenides," *Nature Nanotech*, vol. 12, no. 8, Art. no. 8, Aug. 2017, doi: 10.1038/nnano.2017.100.

[90] J. B. Legma, G. Vacquier, and A. Casalot, “Chemical vapour transport of molybdenum and tungsten diselenides by various transport agents,” *Journal of Crystal Growth*, vol. 130, no. 1, pp. 253–258, May 1993, doi: 10.1016/0022-0248(93)90859-U.

[91] J. You, M. D. Hossain, and Z. Luo, “Synthesis of 2D transition metal dichalcogenides by chemical vapor deposition with controlled layer number and morphology,” *Nano Convergence*, vol. 5, no. 1, p. 26, Sep. 2018, doi: 10.1186/s40580-018-0158-x.

[92] F. Liu, “Mechanical exfoliation of large area 2D materials from vdW crystals,” *Progress in Surface Science*, vol. 96, no. 2, p. 100626, May 2021, doi: 10.1016/j.progsurf.2021.100626.

[93] M. Y. Sayyad, “Synthesis of 2D Janus Crystals and their Superlattices,” p. 128.

[94] T. Meziani, P. Colpo, and F. Rossi, “Design of a magnetic-pole enhanced inductively coupled plasma source,” *Plasma Sources Sci. Technol.*, vol. 10, no. 2, pp. 276–283, May 2001, doi: 10.1088/0963-0252/10/2/317.

[95] Y. Qin *et al.*, “Reaching the Excitonic Limit in 2D Janus Monolayers by In Situ Deterministic Growth,” *Advanced Materials*, vol. 34, no. 6, p. 2106222, 2022, doi: 10.1002/adma.202106222.

[96] H. M. Christen and G. Eres, “Recent advances in pulsed-laser deposition of complex oxides,” *J. Phys.: Condens. Matter*, vol. 20, no. 26, p. 264005, Jun. 2008, doi: 10.1088/0953-8984/20/26/264005.

[97] J. Huotari *et al.*, “Pulsed laser deposition of metal oxide nanostructures for highly sensitive gas sensor applications,” *Sensors and Actuators B: Chemical*, vol. 236, pp. 978–987, Nov. 2016, doi: 10.1016/j.snb.2016.04.060.

[98] Y.-C. Lin *et al.*, “Low Energy Implantation into Transition-Metal Dichalcogenide Monolayers to Form Janus Structures,” *ACS Nano*, vol. 14, no. 4, pp. 3896–3906, Apr. 2020, doi: 10.1021/acsnano.9b10196.

[99] A. Bakin and A. Waag, “3.10 - ZnO Epitaxial Growth,” in *Comprehensive Semiconductor Science and Technology*, P. Bhattacharya, R. Fornari, and H. Kamimura, Eds. Amsterdam: Elsevier, 2011, pp. 368–395. doi: 10.1016/B978-0-44-453153-7.00102-4.

[100] S. Anil, J. Venkatesan, M. S. Shim, E. P. Chalisserry, and S.-K. Kim, “4 - Bone response to calcium phosphate coatings for dental implants,” in *Bone Response to Dental Implant Materials*, A. Piattelli, Ed. Woodhead Publishing, 2017, pp. 65–88. doi: 10.1016/B978-0-08-100287-2.00004-5.

[101] M. N. Bui *et al.*, “Low-energy Se ion implantation in MoS2 monolayers,” *npj 2D Mater Appl*, vol. 6, no. 1, Art. no. 1, Jun. 2022, doi: 10.1038/s41699-022-00318-4.

[102] J. Xu *et al.*, “Unveiling Cancer Metabolism through Spontaneous and Coherent Raman Spectroscopy and Stable Isotope Probing,” *Cancers*, vol. 13, no. 7, Art. no. 7, Jan. 2021, doi: 10.3390/cancers13071718.

[103] Y. P. Varshni, “Temperature dependence of the energy gap in semiconductors,” *Physica*, vol. 34, no. 1, pp. 149–154, Jan. 1967, doi: 10.1016/0031-8914(67)90062-6.

[104] V. Castagnola, “Implantable microelectrodes on soft substrate with nanostructured active surface for stimulation and recording of brain activities,” *undefined*, 2014, Accessed: May 26, 2022. [Online]. Available: https://www.semanticscholar.org/paper/Implantable-microelectrodes-on-soft-substrate-with-Castagnola/7b913e3aa3f76b79ab0873bdf79230ddca24e664

[105] W. Melitz, J. Shen, A. C. Kummel, and S. Lee, “Kelvin probe force microscopy and its application,” *Surface Science Reports*, vol. 66, no. 1, pp. 1–27, Jan. 2011, doi: 10.1016/j.surfrep.2010.10.001.

[106] H. Luo *et al.*, “Interface design for high energy density polymer nanocomposites,” *Chemical Society Reviews*, vol. 48, Jan. 2019, doi: 10.1039/C9CS00043G.

[107] D. Trivedi, “Plasma assisted surface atomic layer substitution for creating Janus 2D materials,” Arizona State University, 2019. Accessed: Jun. 08, 2022. [Online]. Available: https://keep.lib.asu.edu/items/157671

[108] J.-Y. Lee *et al.*, “Evolution of defect formation during atomically precise desulfurization of monolayer MoS2,” *Commun Mater*, vol. 2, no. 1, Art. no. 1, Jul. 2021, doi: 10.1038/s43246-021-00185-4.

[109] H. Taghinejad *et al.*, “Strain relaxation via formation of cracks in compositionally modulated two-dimensional semiconductor alloys,” *npj 2D Mater Appl*, vol. 2, no. 1, Art. no. 1, Apr. 2018, doi: 10.1038/s41699-018-0056-4.

[110] P. Man, D. Srolovitz, J. Zhao, and T. H. Ly, “Functional Grain Boundaries in Two-Dimensional Transition-Metal Dichalcogenides,” *Acc. Chem. Res.*, vol. 54, no. 22, pp. 4191–4202, Nov. 2021, doi: 10.1021/acs.accounts.1c00519.

[111] H. Li *et al.*, “Anomalous Behavior of 2D Janus Excitonic Layers under Extreme Pressures,” *Advanced Materials*, vol. 32, no. 33, p. 2002401, 2020, doi: 10.1002/adma.202002401.

[112] W. N. Hansen and G. J. Hansen, “Standard reference surfaces for work function measurements in air,” *Surface Science*, vol. 481, no. 1, pp. 172–184, Jun. 2001, doi: 10.1016/S0039-6028(01)01036-6.

[113] X. Wang *et al.*, “Defect Heterogeneity in Monolayer WS2 Unveiled by Work Function Variance,” *Chem. Mater.*, vol. 31, no. 19, pp. 7970–7978, Oct. 2019, doi: 10.1021/acs.chemmater.9b02157.

[114] T. Zheng *et al.*, “Excitonic Dynamics in Janus MoSSe and WSSe Monolayers,” *Nano Lett.*, vol. 21, no. 2, pp. 931–937, Jan. 2021, doi: 10.1021/acs.nanolett.0c03412.

[115] C. Kastl *et al.*, “Effects of Defects on Band Structure and Excitons in WS2 Revealed by Nanoscale Photoemission Spectroscopy,” *ACS Nano*, vol. 13, no. 2, pp. 1284–1291, Feb. 2019, doi: 10.1021/acsnano.8b06574.

[116] A. Niebur, T. Lorenz, M. Schreiber, G. Seifert, S. Gemming, and J.-O. Joswig, “Localization of edge states at triangular defects in periodic $\mathrm{Mo}{\mathrm{S}}_{2}$ monolayers,” *Phys. Rev. Materials*, vol. 5, no. 6, p. 064001, Jun. 2021, doi: 10.1103/PhysRevMaterials.5.064001.

[117] Y. Wang *et al.*, “Defects engineering induced room temperature ferromagnetism in transition metal doped MoS2,” *Materials & Design*, vol. 121, pp. 77–84, May 2017, doi: 10.1016/j.matdes.2017.02.037.

[118] H. Xu *et al.*, “Oscillating edge states in one-dimensional MoS2 nanowires,” *Nat Commun*, vol. 7, no. 1, Art. no. 1, Oct. 2016, doi: 10.1038/ncomms12904.

[119] W. Yao, S. A. Yang, and Q. Niu, “Edge States in Graphene: From Gapped Flat-Band to Gapless Chiral Modes,” *Phys. Rev. Lett.*, vol. 102, no. 9, p. 096801, Mar. 2009, doi: 10.1103/PhysRevLett.102.096801.

[120] K. Lingam, R. Podila, H. Qian, S. Serkiz, and A. M. Rao, “Evidence for Edge-State Photoluminescence in Graphene Quantum Dots,” *Advanced Functional Materials*, vol. 23, no. 40, pp. 5062–5065, 2013, doi: 10.1002/adfm.201203441.

[121] L. Tao *et al.*, “Experimental and theoretical evidence for the ferromagnetic edge in WSe 2 nanosheets,” *Nanoscale*, vol. 9, no. 15, pp. 4898–4906, 2017, doi: 10.1039/C7NR00410A.

[122] H. Li *et al.*, “Optoelectronic crystal of artificial atoms in strain-textured molybdenum disulphide,” *Nat Commun*, vol. 6, no. 1, Art. no. 1, Jun. 2015, doi: 10.1038/ncomms8381.

[123] W.-J. Yin *et al.*, “Recent advances in low-dimensional Janus materials: theoretical and simulation perspectives,” *Materials Advances*, vol. 2, no. 23, pp. 7543–7558, 2021, doi: 10.1039/D1MA00660F.